ADVANCED FUNCTIONAL MATERIALS
www.afm-journal.de

Bioprinting Macroporous Hydrogel with Aqueous Two-Phase Emulsion-Based Bioink: In Vitro Mineralization and Differentiation Empowered by Phosphorylated Cellulose Nanofibrils

Qingbo Wang, Özge Karadas, Jessica M. Rosenholm, Chunlin Xu, Tuomas Näreoja, and Xiaoju Wang**

Aqueous two-phase emulsion (ATPE)-based bioinks, a creative innovation for bioprinting, enable the fabrication of complex 3D cell-laden hydrogels with macroporous structure, which promote cellular activities within the scaffold. However, these bioinks intrinsically lack stability and specific biofunctionality, potentially limiting their application for targeted tissue engineering. This study proposes a new perspective by introducing less than 0.1% phosphorylated cellulose nanofibrils (pCNF), a 1D nanofibril top-down produced from natural biomasses, into a dextran/methacrylated gelatin (GelMA)-based ATPE system for extrusion-based bioprinting of preosteoblastic cells, aiming to fabricate macroporous hydrogels with osteogenic differentiation potential. The pCNF that is selectively partitioned in the GelMA phase can not only improve the emulsion stability and alter the rheological behaviors of the ATPE-based bioink, but also enhance the damping capacity and mineralization ability of the crosslinked hydrogels. Furthermore, macroporous hydrogels with pCNF demonstrate increased cell activity and higher viability in post-printing, along with higher alkaline phosphatase activity and osteoblastic gene expression. Importantly, the organized interfaces within the hydrogel facilitate the formation of macroscopic biomineralized nodules in vitro. The incorporation of multifunctional pCNF in the ATPE system significantly boosts the physiochemical and biological performance of the macropore-forming bioink, transforming them into a suitable platform for engineering in vitro bone models.

1. Introduction

Bioprinting has emerged as an innovative technology in tissue engineering and regenerative medicine, enabling the fabrication of complex 3D constructs composed of living cells and biomaterials.[1–3] The design of bioinks is critical, as the bioinks facilitate the creation of complex and functional structures in additive manufacturing and promote the activity of encapsulated cells.[4] Various bioink systems, employing diverse materials, crosslinking methods, and bioprinting techniques have been designed to replicate the properties of specific tissues.[5,6] Among these, aqueous two-phase emulsion (ATPE)-based bioinks have raised significant interest due to their cytocompatibility, versatility, tunability, and particularly, the ability to create interconnected macropores.[7] Nevertheless, challenges remain to be addressed in optimizing the emulsion stability, flow behaviors, and cellular responses to facilitate their use in advanced tissue engineering.

The most used ATPE-based bioinks are primarily composed of the photocrosslinkable methacrylated gelatin

Q. Wang, C. Xu, X. Wang
Laboratory of Natural Materials Technology
Åbo Akademi University
Henrikinkatu 2, Turku FI-20500, Finland
E-mail: Xiaoju.Wang@abo.fi

Ö. Karadas, J. M. Rosenholm, T. Näreoja, X. Wang
Pharmaceutical Sciences Laboratory
Åbo Akademi University
Tykistökatu 6A, Turku FI-20520, Finland
E-mail: tuonar@utu.fi

T. Näreoja
Department of Life Technologies
Faculty of Technology
University of Turku
Kiinamyllynkatu 10 D, Turku FI-20520, Finland

T. Näreoja
Division of Pathology
Department of Laboratory Medicine
Karolinska Institute
Alfred Nobels Allé, 8, Stockholm 14152, Sweden

The ORCID identification number(s) for the author(s) of this article can be found under https://doi.org/10.1002/adfm.202400431

DOI: 10.1002/adfm.202400431

(GelMA) phase and the porogen phase.[7,8] They retain advantages associated with GelMA, such as biocompatibility and thermo-dependent flow behavior, which facilitates cell mixing and guarantees the desired rheological properties for different bioprinting methods.[9–11] A key innovation of ATPE-based bioinks is their ability to form interconnected and macroporous structures, which enhances mass transfer and cellular activities and is superior to the corresponding bulk hydrogel. Also, it allows relatively precise control of the macropore size by adjusting the polymer properties, such as ratio, molecular weight, and source.[8] However, ATPE-based bioinks face the stability challenge due to the lack of inter-droplet repulsion, which leads to rapid creaming even in seconds.[12] Notwithstanding, the mechanical performance of the hydrogels is largely determined by GelMA, such as concentration, methacrylation degree, source, and sterilization method, and might not readily adapt to the increasing demand for customized bioinks.

The advantages of ATPE-based bioinks have motivated intense research endeavors with different strategies to improve their performance while preserving their biocompatibility.[8,13,14] One strategy is altering the properties of the porogen phase. Yi et al. conducted a comprehensive and systematic study and demonstrated that using polyvinyl alcohol and dextran with higher molecular weight as the porogen phase could improve the stability of ATPE-based bioinks.[8] Additionally, applying anionic biosurfactants of rhamnolipids can effectively stabilize PEO/GelMA emulsion by reducing the interfacial tension.[15] Our previous study also demonstrated using a water-soluble non-ionic polysaccharide derivative as an emulgator to improve the emulsion stability by co-partitioning in both GelMA and dextran phases.[16] Another effective strategy is the Pickering emulsion method by applying biocompatible nanoparticles that settle on the interface and form a barrier to prevent droplet coalescence.[13,14] Pickering emulsion could not only improve the stability of the ATPE-based bioinks but also offer multifunctionality by specifically tailoring the nanoparticles. For example, Wang et al. utilized interleukin-4-loaded Ag-coated Au-nanorods (IL-4@AgGNRs) that endowed the bioinks with antimicrobial properties and anti-inflammatory regulation.[14]

Cellulose nanofibrils (CNF), fibrous 1D nanomaterials derived from renewable lignocellulosic sources, have demonstrated exceptional network-forming ability and biocompatibility, making them valuable additives for enhancing different biomaterial systems.[17–20] In addition, surface hydroxyl groups of CNF offer chemical accessibility, and their derivatives with diverse functionalities have been customized to biomedical utilizations.[21,22] Inspired by peer studies on enhancing the stability of ATPE-based bioinks, our paper presents a novel approach that utilizes phosphorylated cellulose nanofibrils (pCNF) as a multifunctional additive to enhance the stability and bioactivity of dextran/GelMA-based ATPE bioinks, as illustrated in **Figure 1**. Compared to molecule-assembled micelles or 0D nanomaterials, pCNF with a high aspect ratio is anticipated to form an entangled secondary network within the GelMA phase, even at low concentrations. The pCNF network should not only act as a spatial barrier to prevent the creaming of the dextran droplets, but also offer broad control over the bioinks' rheological properties, and help prevent cell sedimentation during bioink preparation.[23–25] Applying a secondary and physically entangled pCNF network within the GelMA might contribute to stress dissipating to enhance the durability of the hydrogel, without disrupting the macropore formation.[26]

Bioprinted hydrogels have been recognized as a promising platform for studying bone remodeling, due to their similarity to the natural extracellular matrix (ECM).[27] The essential properties of such a bioink system shall facilitate hydrogel fabrication with robust bioprintability and high macroporosity. Furthermore, bioinstructive scaffolds, which present specific cues to guide cellular behavior in the 3D environment post-bioprinting, are highly demanded.[28–30] In in vitro 3D cell culture, using a medium with osteogenic supplements is a common practice to induce osteogenic differentiation.[31,32] Adding inorganic phosphate (Pi) has been proven to induce osteogenic differentiation through the non-canonical Wnt pathway in the early stage and by Akt/mTORC1 pathway.[33–36] Recent studies have shown that using phosphorylated biopolymers (e.g., chitosan or alginate) for composite hydrogel fabrication could regulate osteogenic and chondrogenic differentiation, due to their functional similarity to phosphorous groups in natural bone and cartilage.[37–41] Thus, from the perspective of tuning the substrate compositions for integrated biological functionalities, the incorporation of pCNF in ATPE-based bioink is hypothesized to provide nucleation sites through the surface phosphates as an insoluble factor to promote mineral growth and potentially induce the osteogenic differentiation in the ATPE-based hydrogels.

The present study systematically describes the effect and functionalities when introducing the 1D surface-charged pCNF into ATPE, referring to i) its partition behavior upon changes in ionic strength at physiological pH; ii) its influence on ATPEs and hydrogels properties, including stability, rheological and mechanical characteristics; iii) its impact on cellular activity in extrusion-based bioprinting; and iv) the effect of its surface-presented phosphates on the osteogenic differentiation and biomineralization. As a proof of concept, the pCNF-containing ATPE (p_ATPE) hydrogel with both structural and chemical mimicry is established for engineering in vitro bone models with osteogenic differentiation ability.

2. Results and Discussion

CNF, as a class of 1D nanofibril biopolymers, has shown excellent performance in stabilizing oil/water and aqueous emulsions.[23,42] Their network-forming capacity in aqueous conditions, driven by the strong negative charge repulsion and fibril entanglement, is highly favored as a Pickering emulsion stabilizer. The abundant phosphate groups introduce a high negative charge on the pCNF surface that enables uniform aqueous dispersion. However, the anionic CNF network is sensitive to cations, which can disrupt the electrostatic interactions between the nanofibrils and lead to fiber flocculation. Therefore, when incorporating pCNF into ATPE-based bioinks, understanding the impact of monovalent cations (e.g., Na^+ in PBS) on the pCNF network morphology, and the pCNF partitioning behavior between the two phases becomes more crucial. To gain insights into the pCNF partitioning behavior, we conducted the confocal microscopy analysis on the ATPE-based inks, as illustrated in **Figure 2a,b**. When ATPE-based inks were prepared using PBS containing ≈150 mM of NaCl, a clear emulsion was yielded

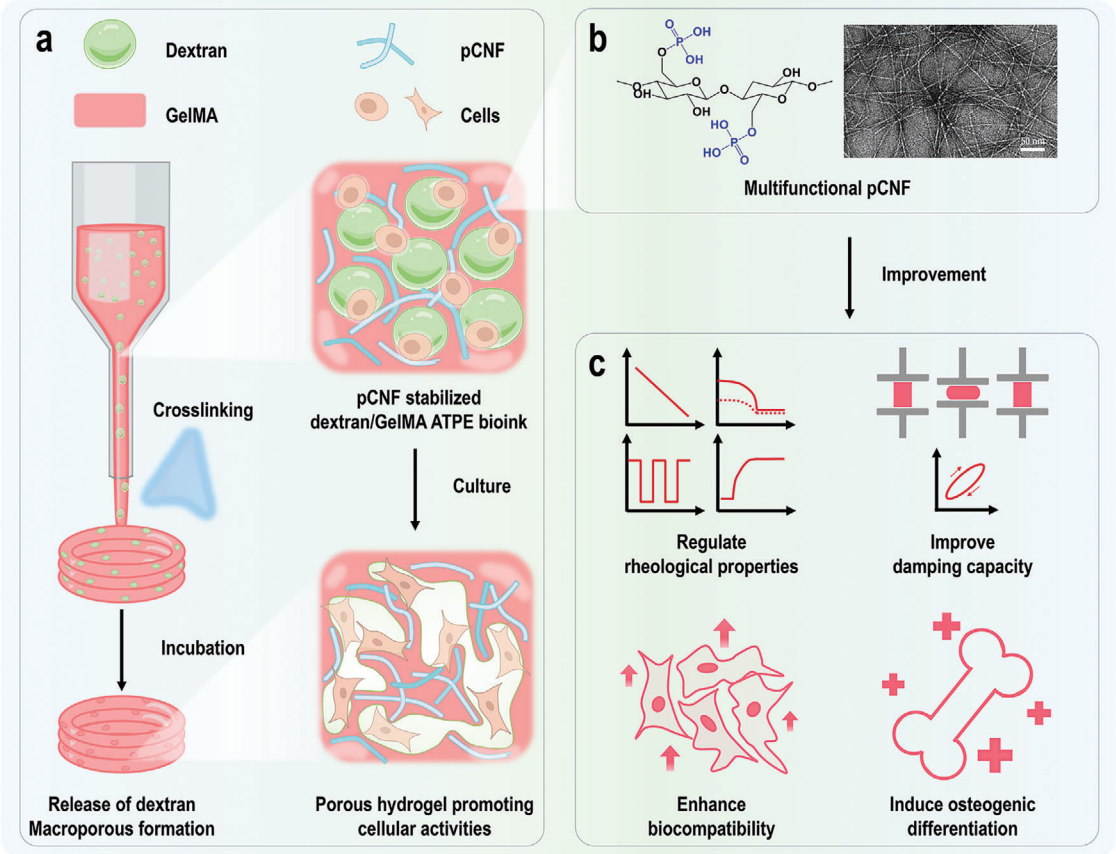

Figure 1. a) Schematic illustration of the bioprinting process using p_ATPE bioink. b) Chemical structure and representative TEM image of the pCNF. c) Improvement of the bioinks by incorporating pCNF. Scale bars for Figure 1b: 50 nm.

(Figure 2a(i)) with individual dextran (green) microdroplets forming in the GelMA (red) phase. Upon introducing pCNF by dissolving GelMA in pCNF dispersion and then mixing them with dextran solution, phase separation between the GelMA and dextran phases remained, as illustrated in Figure 2a(ii–iv). However, the regular shape of the dextran phase was largely disturbed upon the addition of pCNF, and severe flocculation of pCNF was observed. Moreover, the fluorescence signal from pCNF (blue) largely overlapped with the dextran phase and separated from the GelMA phase, as illustrated by the cyan color. The macropore-forming ability of ATPE-based bioinks is attributed to the leaching of the uncrosslinked dextran phase during cell culture. However, macropore formation could be hindered when PBS is used to prepare p_ATPE inks since the space was occupied by the flocculated pCNF, as illustrated in Figure 2a(v). Moreover, pCNF flocculation might cause nozzle clogging problems during extrusion-based printing. The primary functions of PBS are to maintain pH and balance osmolarity between cells and bioink, which are vital for cell viability and activity. However, the high ionic strength of PBS deteriorates the uniformity and stability of the pCNF network and disrupts the macropore formation owing to the pCNF partition in the dextran phase. This leads to an irreversible decrease in printability and cytocompatibility of the ATPE-based inks. To address this issue, low ionic strength 20 mM HEPES buffer supplemented with mannitol was selected for bioink formulating, which could maintain the pH and osmolarity of the bioink for cells, while minimizing the effect of ionic strength on pCNF network stability.

ATPE-based inks prepared in HEPES buffer exhibited smaller dextran droplet sizes compared to those prepared in PBS buffer (Figure 2b(i)). A similar emulsifying phenomenon between GelMA and dextran phases was still visible when 0.05% pCNF was added to Lp_ATPE inks (Figure 2b(ii)). Noteworthy, when increasing the pCNF concentration to 0.075 and 0.1%, the emulsifying phenomenon was different as the dextran droplets deformed, resulting in formation of a bicontinuous GelMA network, as shown in Figure 2b(iii and iv). Notably, pCNF exhibited completely different partition behaviors in low and high ionic strength buffers. pCNF in HEPES buffer is selectively partitioned within the GelMA phase instead of in the dextran phase (Figure 2b(ii–iv)), likely attributed to the electrostatic attraction between the negatively charged pCNF and the positively charged part of GelMA molecules.[43] We further investigated the sequence of dissolving components during ink preparation to determine whether it could affect pCNF partition behavior. The results showed that pCNF eventually migrated to the GelMA phase even when pCNF was initially dissolved in dextran and subsequently mixed with GelMA solution (Figure S1, Supporting Information). When formulating the inks using PBS, the negative charge of pCNF can be screened by the Na^+ and entangled into

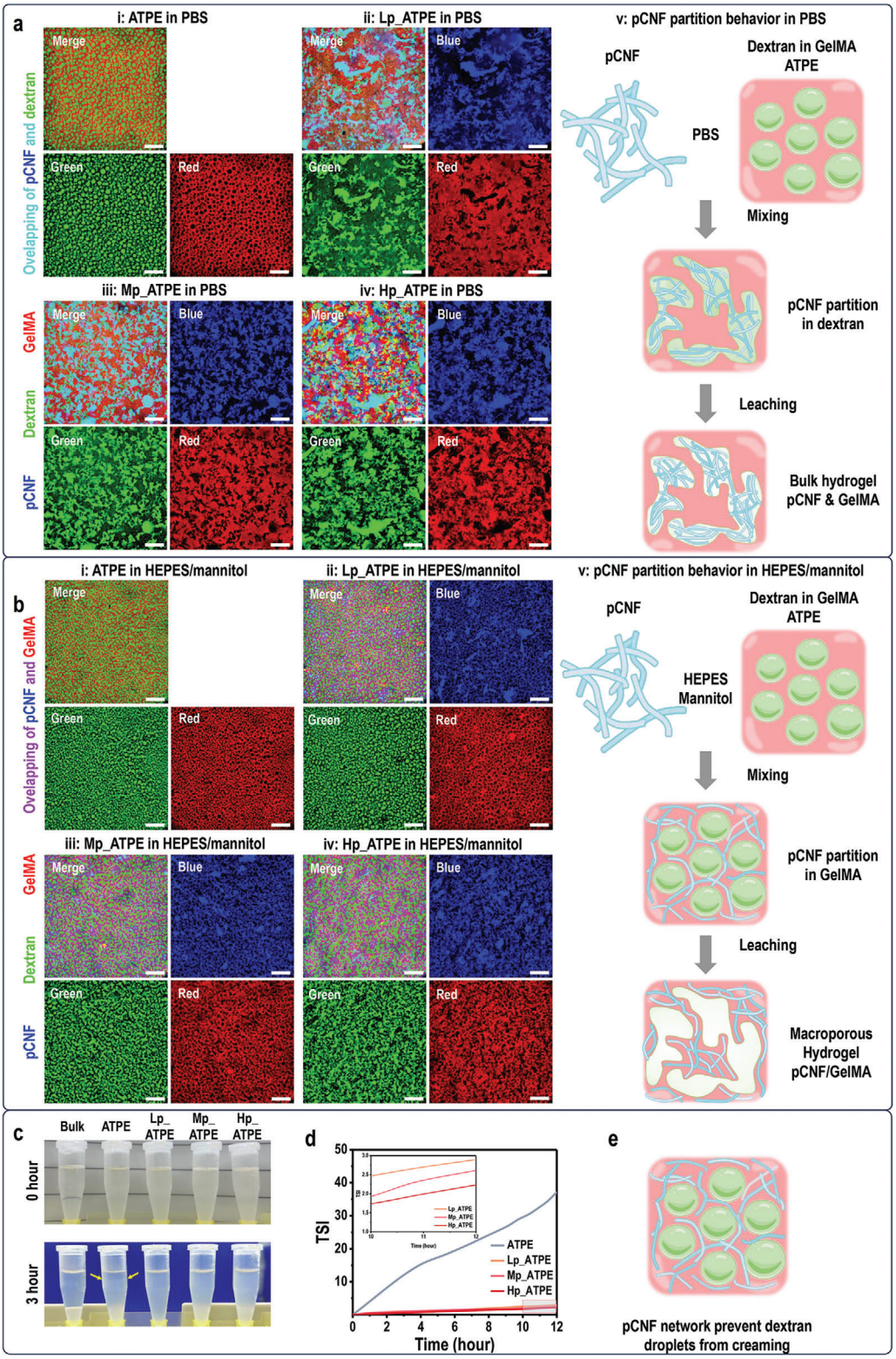

Figure 2. pCNF partitioning behavior in the ATPE and enhanced stability of p_ATPE inks. a,b) (i to iv) Representative fluorescence microscopy images of the ATPE-based inks, (v) illustrating different pCNF partitioning behavior in (a) PBS and (b) HEPES/mannitol buffer. (pCNF marked with blue fluorescence; dextran marked with green fluorescence; GelMA marked with red fluorescence; overlapping pCNF and dextran observed as cyan; overlapping pCNF and GelMA observed as magenta) c) Representative images of the inks after standing at 37 °C for 0 and 3 h. Clear phase separation between GelMA and dextran without pCNF occurs after 3 h as indicated by the yellow arrows. d) TSI curves of the ATPE-based inks. e) Illustration of the improvement in ATPE stability upon incorporation of pCNF. Scale bars for Figure 2a,b: 200 µm.

weak flocs. The pCNF flocs would further migrate to the dextran phase, likely due to their chemical structural similarity. Similar behavior was also reported in the dextran/polyethylene oxide emulsion stabilized by cellulose nanocrystals (CNC). CNC was found to show a strong preference for the dextran phase when the two phases are both non-charged.[44] In bioprinting, the engagement of negatively charged pCNF with the GelMA phase at low ionic strength preserves the macropore-forming ability of the p_ATPE inks, as illustrated in Figure 2b(v).

The stability of p_ATPE inks is an important attribute for assessing their properties and suitability in bioprinting applications. For the ATPE-based inks with or without pCNF, the ultralow interfacial tension between the two phases of ATPE allows ink emulsification by simply vortexing for 5–10 s (Figure 2c). However, the ultralow interfacial tension also makes the stabilization of ATPE ink challenging. After standing at 37 °C for 3 h, the ATPE ink showed a clear phase separation (see yellow arrows in Figure 2c). In contrast, no phase separation was observed in the p_ATPE inks in visual inspection (Figure 2c). To quantify the effect of pCNF on the stability of dextran/GelMA-based ATPE inks, the stability of the ATPE-based inks was monitored by the turbiscan stability index (TSI) values measured at 37 °C. As shown in Figure 2d and Figure S2 (Supporting Information), the ATPE ink displayed a highly unstable profile, in which the TSI exceeds 10 after 2.5 h, indicating the destabilization of the ATPE ink, and the TSI further increased to 35.6 after 12 h of standing. In contrast, all the p_ATPE inks were more stable, with TSIs below 3 after 12 h of standing. Additionally, the stability was further improved as pCNF concentration increased from 0.05 to 0.1%, where the TSI decreased from 2.90 to 2.23. It is assumed that pCNF with a high aspect ratio is selectively dispersed in the GelMA phase and forms a network as a physical barrier that further prevents the coalescence of dextran droplets and enhances the emulsion stability, as illustrated in Figure 2e. Biocompatible 0D nanoparticles have been attributed with the capability to stabilize ATPE-based inks due to the Pickering effect.[13,45] Similarly, 1D pCNF with a high aspect ratio was confirmed to stabilize the GelMA-dextran interface.

The rheological properties of bioinks play a pivotal role in determining their overall performance in bioprinting, especially for extrusion-based bioprinting should meet a series of rheological properties of shear-thinning, rapid recovery, and immediate crosslinking responsiveness.[46] The thermal-dependent sol–gel transition of GelMA is highly beneficial for bioprinting, and the ATPE-based inks also maintain these properties as shown in **Figure 3**a. Comprehensive rheological characterizations were performed to investigate the effect of pCNF on the rheological properties of dextran/GelMA ATPE inks. We first tested the flow curves of the inks at 15 °C, within the common temperature range to conduct bioprinting for GelMA-based inks. As shown in Figure 3b(i and ii), all the inks showed a shear-thinning profile with the power law index n below 1, which facilitates the ink extrusion through the nozzle. The resistance of flow, indicated by k, of all the ATPE-based inks, were significantly lower compared to bulk ink (Figure 3b(iii)). This might be attributed to the fact that the bulk ink has only a one-phase structure of gelated GelMA, whereas the ATPE-based inks contain two phases of both the gelated GelMA phase and the free-flowing dextran phase. The heterogeneous internal structure of ATPE-based inks exhibits low resistance to flow as shown in Figure 3b, which might be beneficial for cell viability in extrusion-based bioprinting. The lower shear stress during printing can minimize the potential damage to the cells.[47] The flow behavior of ATPE-based inks at 15 °C is mainly dominated by the thermal responsive GelMA, and the addition of pCNF did not increase the flow resistance (Figure 3b(iii)). All three p_ATPE inks showed similar flow behavior, independent of the pCNF concentration. Compared to ATPE ink, the p_ATPE inks showed lower viscosity at a low shear rate region and slightly higher viscosity at a very high shear rate region, this might be due to the alignment-disorder process of the pCNF upon shearing.

Conversely, at 25 °C, a common practice temperature, inks exhibited distinct flow behavior than that at 15 °C. All the inks showed a drastic decrease in viscosity, where the k decreased for almost 3 orders of magnitude (Figure 3c(iii)). Moreover, both bulk and ATPE ink exhibited an almost Newtonian behavior, where the n values are close to 1 (Figure 3c(ii)). However, p_ATPE inks still exhibited a shear-thinning behavior at 25 °C, and the viscosity increased with the concentration of pCNF (Figure 2b). This is owing to the excellent network-forming ability of pCNF within the GelMA phase. The low viscosity facilitates cell mixing through gentle pipetting and enables even distribution of cells within the bioink. However, the low viscosity of the bioink, like the bulk and ATPE bioinks, might raise concern as the cells tend to rapidly sediment to the bottom.[48] Aided by the pCNF network formed by nanofibril entanglement, the p_ATPE bioinks transformed into a weak gel state without additional crosslinking that did not hinder the cell mixing process, while ensuring the cells were suspended.[49] The weak gel network was further evidenced by the temperature sweep, as shown in Figure 3d. Notably, even though the viscoelasticity of the Mp_ and Hp_ATPE ink decreased with the increase in temperature, they did not display a sol–gel transition within the temperature test range, where the storage modulus (G') is still slightly higher than loss modulus (G'') up to 40 °C, indicating a weak gel network.

During extrusion, the inks undergo a shear-thinning and relaxation process. The rapid shear recovery property allows the extrudate to maintain the structure without spreading, assuring printing fidelity. We further conducted the shear recovery measurement at 15 °C. As shown in Figure 3e, all the inks exhibited a rapid shear recovery, with G' reaching a plateau within 2 s after relaxation. Meanwhile, the bulk ink showed a relatively poor shear recovery property with G' recovery of 75.9% and 71.3% after the initial and secondary shear, respectively. In contrast, all the ATPE-based inks showed better shear recovery properties, with over 94% G' recovery achieved in both initial and secondary shear. The lower G' of ATPE ink compared to bulk ink at rest and higher G' at recovery might be owing to the energy-dissipating ability of flexible dextran droplets that deform under high shear and return to the original shape at relaxation. Moreover, the p_ATPE inks exhibited near instantaneous and complete recovery behavior with a recovery of at least 97.6% and higher G' than ATPE ink, which is mainly attributed to the presence and reorganization of the pCNF network within the GelMA phase.

After extrusion, the inks remained responsive to efficient crosslinking that improved the mechanical properties and the prints could bear the weight of subsequent layers. All ATPE-based inks showed a rapid crosslinking response, with the G'

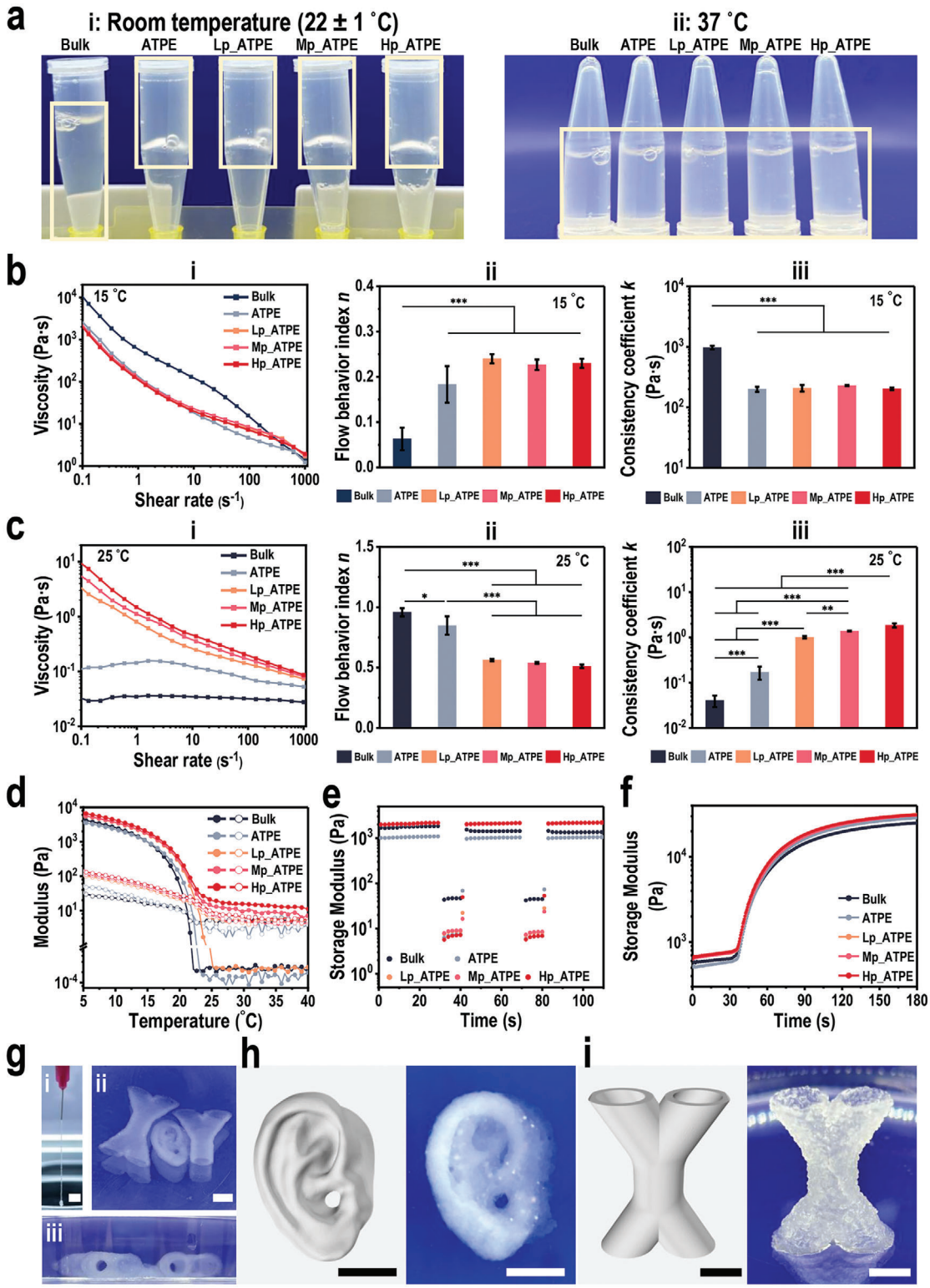

Figure 3. Rheological characterization and printability demonstration of inks. a) The sol–gel transition of the inks at (i) room temperature (22 ± 1 °C) and (ii) 37 °C (Ink position in the tube is labeled in the yellow box). b,c) Flow behaviors of the inks at 15 and 25 °C. (i: flow curves, ii: flow behavior index *n*, iii: consistency coefficient *k*). d) Gelation behaviors of the inks determined by temperature sweep measurements. (close symbol: *G′*; open symbol: *G″*). e) Shear recovery properties of inks at 15 °C. f) Photo-crosslinking profiles of the inks at 15 °C, illustrating their crosslinking kinetics and mechanical properties of the crosslinked hydrogel. g) i: Continuous extrusion of Lp_ATPE inks, illustrating their ability to hold the structure after extrusion. Representative images from (ii) front and (iii) side views of printed structure immersed in PBS after 7 days. h,i) Representative images of the printed centimeter-scale hydrogels with complex structures (human ear and X-shaped hollow tubes). Statistical analysis: $^{*}p < 0.05$, $^{**}p < 0.01$, $^{***}p < 0.001$, $n = 3$. Scale bars for Figure 3g–i: 5 mm.

increasing within 6 s after the light exposure, as shown in Figure 3f. The pCNF increases the G' of the p_ATPE inks both prior to and after the light exposure, without hindering the crosslinking kinetics. Through the comprehensive rheological characterization, we present how the incorporation of the pCNF network improves ATPE-based inks' rheological properties related to the bioprinting process. CNF is known for its ability to form an entangled and reversible network through van der Waals forces, hydrogen bonding, and electrostatic interactions.[50] High concentrations of CNF have been used as a rheological modifier in bioink development to improve the extrudability of hyaluronan-based bioink, where CNF provides great shear recovery with a rapid response.[46] However, the destabilization of CNF by ions is more severe at higher concentrations, and even low ionic strength results in a hysteresis behavior even at the initial shear.[18] In our study, the minimal concentration of pCNF (0.05–0.1%) formed a weak, less entangled network in GelMA phase that did not weaken the network strength of ATPE inks between relaxation and after shearing, but improved their viscoelasticity through polymer interactions. The rheological results further support the hypothesis that the pCNF network acts as a spatial barrier for dextran droplets thus enhancing the stability. Overall, pCNF serves as an effective rheology modifier and ATPE stabilizer and could benefit the bioprinting and post-bioprinting process of the ATPE bioinks.

To demonstrate the printability and printing fidelity of p_ATPE inks in extrusion-based 3D printing, complex centimeter-scale 3D structures were fabricated using Lp_ATPE ink. The printing parameters of the inks were determined based on their consistent extrusion under a similar environment. As shown in Figure 3g(i), a continuous 36 mm filament can be extruded out of the nozzle, indicating the ink's ability to maintain filament fidelity during the extrusion-based printing process, which is critical to ensure printing accuracy.[51] We analyzed the printability of the inks using printability (Pr) value, as shown in Figure S3 (Supporting Information). The bulk ink showed a highly gelated state with a Pr value of 1.32 ± 0.10. In contrast, all the ATPE-based inks showed a Pr value slightly higher than 1, indicating better shape fidelity with a lightly gelated status. Adding pCNF did not significantly change its Pr value, since the ATPE inks already possessed great printability. Though Lp_ATPE ink showed a Pr value closest to 1, the difference was not significant compared to ATPE ink. Then, a human ear model with a size of $\approx 15 \times 10.5 \times 4.3$ mm^3 was successfully printed using Lp_ATPE ink, which also demonstrated its applicability for printing computer-aided design models (Figure 3h). Additionally, we printed a slightly challenging X-shaped hollow tube model with a size of $\approx 15 \times 6 \times 20$ mm^3 (wall thickness of 0.75 mm). The result shows that the Lp_ATPE ink can support the printing of such a complex model with a relatively high aspect ratio and thin wall thickness, particularly the free-standing upper geometry in extrusion-based 3D printing (Figure 3i; Movie S1, Supporting Information). The printed structure showed structural stability while being immersed in PBS for several weeks without deforming (Figure 3g(ii and iii)).

To investigate the effect of pCNF on the hydrogel mechanical properties, the compressive stress-strain profiles of cast hydrogel cylinders were compared in **Figure 4a**. ATPE hydrogels exhibited higher Young's modulus and maximum stress than bulk hydrogel, increasing from 65.6 ± 3.2 to 68.6 ± 1.6 kPa (Figure 4b) and from 145.8 ± 50.7 to 215.1 ± 35.4 kPa (Figure 4c), respectively. This is mainly caused by the increased crosslinking density of GelMA.[7] The Young's modulus of Lp_ATPE hydrogel slightly increased to 71.1 ± 4.9 kPa, but decreased with further addition of pCNF, i.e., Young's modulus of Hp_ATPE hydrogel decreased sharply to 39 ± 2.8 kPa, as shown in Figure 4b. However, the flexibility of the hydrogel increased with increasing the pCNF concentration as the maximum strain gradually increased from $49.3 \pm 2.4\%$ to $58.7 \pm 1.9\%$, when the pCNF concentration increased from 0.05% to 0.1% (Figure 4d). The maximum stress and toughness reached the peak with Mp_ATPE hydrogels at 239.3 ± 36.9 kPa and 28.1 ± 2 kJ m^{-3}, respectively (Figure 4c,e).

The surface phosphate groups on pCNF provide p_ATPE hydrogels an opportunity for further crosslinking with divalent cations present in biological systems. We investigated the effect of Ca^{2+} crosslinking (Ca^{2+}(X)) with pCNF on the mechanical properties. As shown in Figure 4a–e, the mechanical performance of the Ca^{2+}(X) p_ATPE hydrogels remained similar trend to the non-crosslinked hydrogels with a slight increase in the maximum stress and toughness of Ca^{2+}(X) Mp_ATPE hydrogels to 276.5 ± 52 and 30.5 ± 4.6 kPa (Figure 4c,e), respectively. Previous studies have shown that 1D cellulosic nanomaterials are efficient in reinforcing the nanocomposite hydrogel by forming an entangled network.[22,52,53] The accumulated insights reveal the mechanism of pCNF regulating the mechanical properties of ATPE-based hydrogels (Figure 4f). In our hypothesis, when p_ATPE hydrogels are compressed, the entangled pCNF network within GelMA will easily break down, thus resulting in a decrease in Young's modulus. However, this process could effectively dissipate compressive energy, thereby increasing the maximum strain and considerable toughness.[54] Bacterial nanocellulose (BNC), with a larger aspect ratio, was reported to increase Young's modulus of the GelMA hydrogel with a concentration of 0.075–0.5%.[52] This improvement in Young's modulus might be owing to the more entangled network and higher dosage. For example, using 10% cellulose nanocrystal (CNC), with a low aspect ratio that is not ideal for network formation, could still significantly improve Young's modulus of GelMA/HAMA hydrogels.[55] On the other hand, the porous structures showed a great impact on Young's modulus of the hydrogels. As observed in Figure 2b(iii and iv), high pCNF dosage resulted in the formation of a bicontinuous pCNF/GelMA phase in the p_ATPE inks. Compared to the relatively uniform GelMA structure of the bulk and ATPE hydrogels, the bicontinuous pCNF/GelMA network might exhibit greater ductility with a relatively lower Young's modulus but higher strain resistance.

When using anionic nanocellulose as reinforcing additives in an aqueous composite system, a deionized environment is preferred to prevent nanofibril coalescence. This is a technical challenge to address in cell mixing when utilizing nanocellulose of this specialty in bioinks. In this work, we revealed the effect of ionic strength on pCNF partitioning patterns in ATPE-based inks. Also, a conditioning buffer containing HEPES and mannitol was confirmed to have minimal electrostatic interaction with the negatively charged fibers and that maintained the pCNF network stability. Meanwhile, the pCNF partitioning behavior under this buffer condition also contributes to the maintenance of macropores in the hydrogel. Through the incorporation of a minimal amount of pCNF, we could tune the mechanical property to

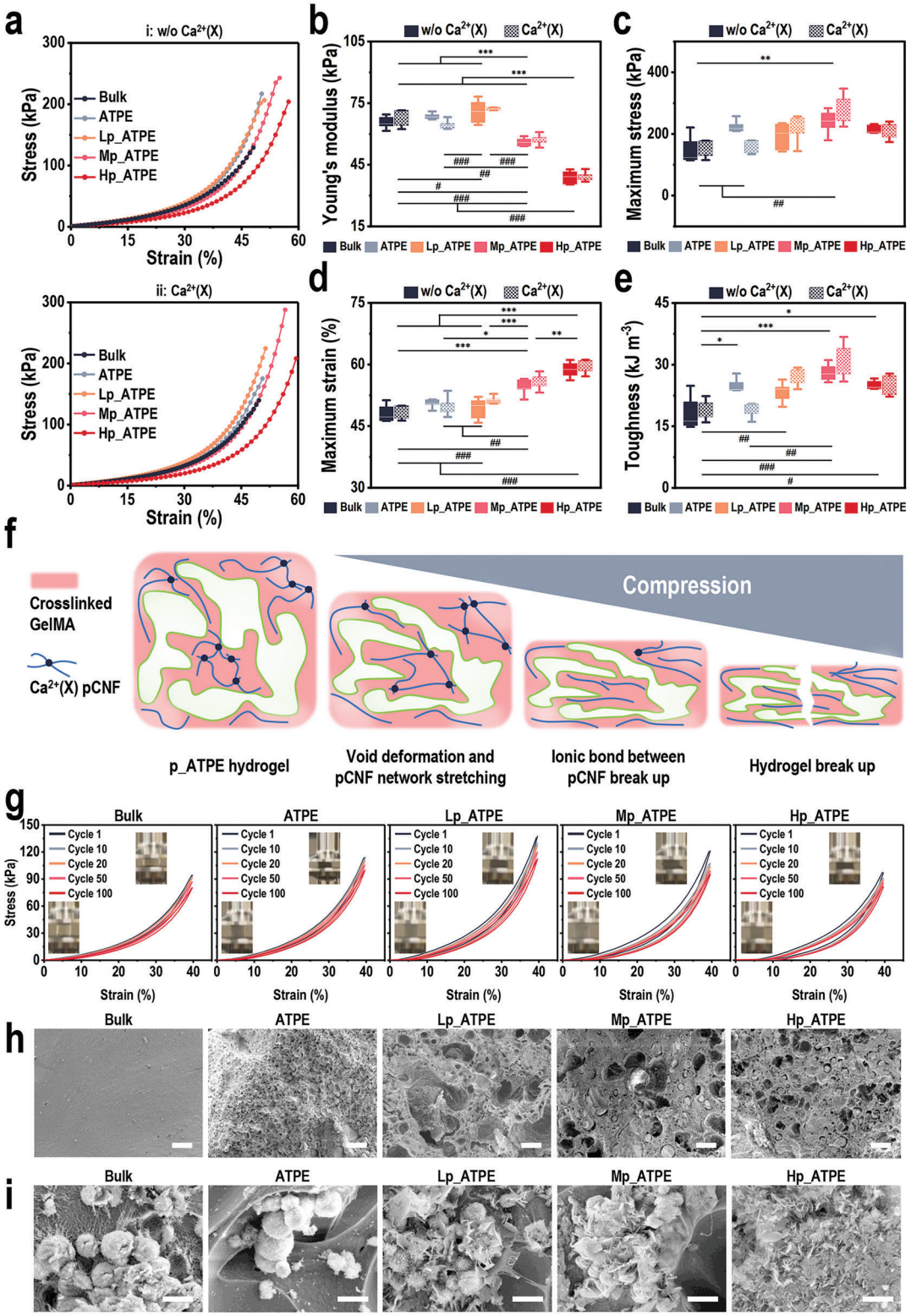

Figure 4. Mechanical properties and morphology of hydrogels. a) Compression stress-strain curves of hydrogels (i) w/o or (ii) with Ca^{2+} crosslinking (Ca^{2+}(X)). b) Young's modulus, c) maximum stress, d) maximum strain, and e) toughness of the hydrogels with or without Ca^{2+} crosslinking. w/o Ca^{2+}(X): $^{*}p < 0.05$, $^{**}p < 0.01$, and $^{***}p < 0.001$; Ca^{2+}(X): $^{\#}p < 0.05$, $^{\#\#}p < 0.01$, and $^{\#\#\#}p < 0.001$, $n > 5$. f) Schematic illustration of the hypothesized fracture process of Ca^{2+}(X) p_ATPE hydrogel upon compression. g) Cyclic compression stress-strain curves of hydrogels at 40% strain for 100 cycles (Inserts show the corresponding hydrogels compressed at 0% and 40% strain). h) Representative SEM images of hydrogel cross-sectional morphology. i) Representative SEM images of the mineralized hydrogels incubated in 10X SBF for 6 h. Scale bars for Figure 4h:100 µm; Figure 4i:5 µm.

a certain extent, which might facilitate the creation of matrix stiffness interfaces for directing cell polarization and differentiation in organoid construction.

The ATPE-based hydrogels with macroporous structures are anticipated to withstand repeated compression as soft tissues, like skin and cartilage. In the cyclic compression test, all the hydrogels showed a great capacity to restore their original shape after 100 cycles of repeated compression, with the unloading curve returning to the original point (Figure 4g). Although, a decrease in maximum stress was observed in all samples after they were compressed 100 times, but no obvious fractures in visual inspection (Movie S2, Supporting Information), indicating a change in the internal network. As shown in Figure 4g, the bulk and ATPE hydrogels showed a small hysteresis loop profile, indicating the highly elastic network formed by covalently crosslinked GelMA. Larger hysteresis loops are observed with the incorporation of pCNF, and the loops get larger as the pCNF content increases (Figure 4g; Figure S4, Supporting Information). This demonstrated the pCNF network's capability to dissipate energy during hydrogel compression, endowed by their entanglement within the bicontinuous structure of p_ATPE hydrogels. This contributes to the improvement in resilience and durability of ATPE hydrogels in long-term applications.

SEM images were taken to visualize the morphology of the lyophilized hydrogel samples. The macroporous structure-forming ability of ATPE-based hydrogels was evidenced in Figure 4h, where the bulk hydrogel showed a flat and dense structure. As shown in Figure 4h, the ATPE hydrogel showed a relatively uniform and small pore structure. With the addition of pCNF, the pores not only became larger in dimension but also reformed into an interconnected channel structure, where the bottom of the pores was too deep to be visible. The hydrogels' ability to promote localized mineralization in vitro was predicted by immersing the hydrogels in 10X SBF for 6 h, followed by intensive washing and drying using the critical CO_2 method to preserve the morphology and integrity of the Ca/P complexes. As illustrated in the SEM images and EDX spectroscopy (Figure 4i; Figure S5, Supporting Information), granular-shaped Ca/P complexes were formed on the surface of the bulk and ATPE hydrogel. As anticipated, the precipitation speed was greatly increased in the p_ATPE hydrogels with the incorporation of pCNF (Figure 4i), with flake-like structure of Ca/P complexes observed with the p_ATPE hydrogels. This phenomenon supported the hypothesis that pCNF could act as nucleation centers for Ca/P complex formation and increase the complexation points for Ca^{2+} to promote further growth.

GelMA-based ATPE bioinks have been well demonstrated with great biocompatibility.[7,14] To confirm the biocompatibility of p_ATPE hydrogels, especially the effect of pCNF on the cell viability, spreading, and proliferation, we performed CCK-8 assay on the MC3T3-E1 cell-laden hydrogels cultured in vitro for 7 days. As shown in **Figure 5**a, the metabolic activity of the encapsulated MC3T3-E1 cells in all the hydrogels showed a similar trend with recovery and a gradual increase in CCK-8 signal by day 3 and proliferation and an increase in cells' activity by day 7. As expected, the ATPE hydrogels showed enhanced biocompatibility compared to the bulk hydrogels attributed to the macroporous structure that facilitates cell spreading and mass transfer.[7,16] The proliferation and the metabolic activity of cells in p_ATPE hydrogels were significantly higher than that in the ATPE hydrogels, especially on day 3, indicating faster recovery of the cells (Figure 5a). To evaluate the cell viability post-bioprinting, we performed the live/dead staining on the bioprinted hydrogels, as displayed in Figure 5b. The printing parameters were not optimized to enhance cell viability but with the goal of ensuring constant extrusion under similar parameters. The bulk hydrogel showed the lowest viability (70.1 ± 12.6% and 65.7 ± 7.3% on days 1 and 3, respectively). The lower cell viability in bulk hydrogels is mainly due to the high ink flow resistance and gelated status of the bulk bioink (Figure 3b; Figure S3, Supporting Information) which results in a more challenging condition for the cells.[56] All the ATPE hydrogels showed a high viability of ≈80% on day 1 throughout the 7 days of culturing period, as shown in Figure 5c. In addition, on day 3, the p_ATPE hydrogels showed significantly higher viability (over 90%) compared to the ATPE hydrogel (83.7 ± 5.8%), further confirming the rapid cell recovery within the p_ATPE hydrogels. Cells are evenly distributed throughout the bioprinted hydrogels, and the green signals are overwhelming and increase with the culturing time (Figure 5e). The result also revealed the advantage of porous ATPE-based hydrogels, where the encapsulated cells showed a spindle-like shape in ATPE hydrogels rather than those that remained predominantly spherical in the bulk hydrogel. The cytoskeletal staining (Figure 5f) further validated the spreading of MC3T3-E1 in the bioprinted hydrogels after 7 days of culture. The metabolic activity and viability of bioprinted MC3T3-E1 cells suggested that pCNF significantly enhanced the cytocompatibility of the ATPE bioinks, and created a suitable environment throughout the bioprinting process, which promoted the cellular activities of the encapsulated cells. The high cell viability on day 1 also indicates that the HEPES and mannitol buffer system used in bioink preparation did not show a negative effect on the cells.

Biomaterials that are designed for the generation of bone tissue should be osteoinductive and osteoconductive for promoting the osteogenic differentiation of stem cells and also promote mineralization within the construct. To assess the osteoinductivity of the bioinks, alkaline phosphatase (ALP) enzyme activity, an indicator of early osteogenic differentiation, was measured in bioprinted MC3T3-E1 cells cultured in a normal culture medium without additional osteogenic stimulus. As shown in Figure 5d, there was no significant difference between the ALP activity of bioprinted hydrogels on day 7. However, by day 14, ALP activity of cells had increased in all the hydrogels, and moreover, this increase was significantly higher in p_ATPE hydrogels compared to the bulk and ATPE hydrogels, indicating the pronounced osteogenic stimulation by pCNF. Catalytic reactions in the body result in ATP hydrolysis that leads to the release of inorganic pyrophosphates as a substrate for ALP enzyme which is converted into Pi. The local Pi concentration increase drives the precipitation with calcium ions and initiates the mineralization process. Previous research showed that substrate surface phosphorus groups can induce osteogenic differentiation even without chemical induction by the addition of osteogenic supplements, presumably as a response to return the amount of inorganic phosphorus in the system back to the physiological level.[57,58] Our results are consistent with those findings, in which p_ATPE hydrogels showed the highest ALP enzyme activity on day 14. The activity was similar for all p_ATPE hydrogels, for Lp_ATPE

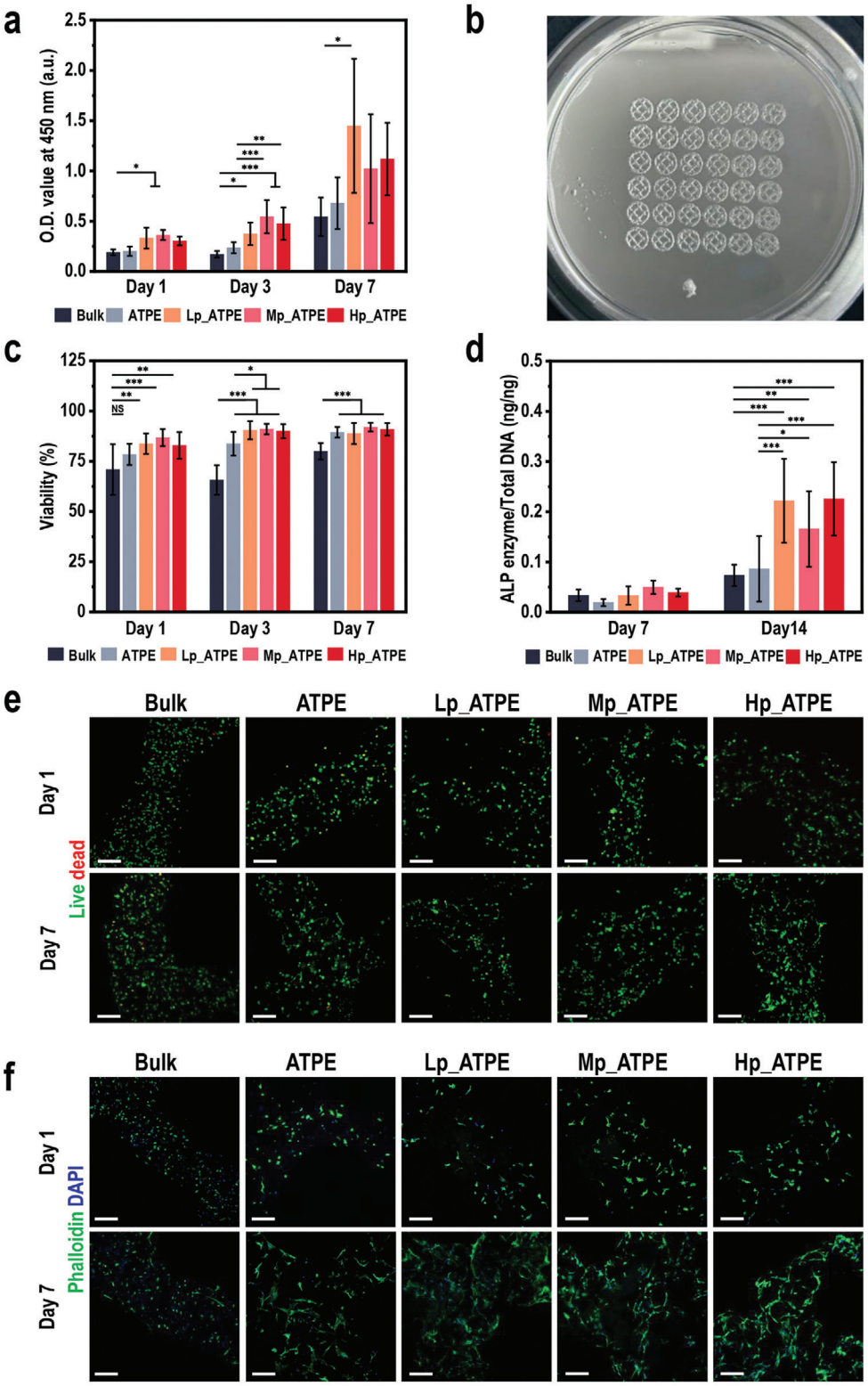

Figure 5. Cytocompatibility analysis of hydrogels and bioprinting using MC3T3-E1 cells. a) CCK-8 assay of the MC3T3-E1 cells laden hydrogels during 7 days culture. b) Representative images of bioprinted MC3T3-E1 cells laden hydrogels (Lp_ATPE) with good consistency and shape fidelity on a 100 mm petri dish. c) Viability of MC3T3-E1 cells in the bioprinted hydrogels on days 1, 3, and 7. d) ALP enzyme activity of MC3T3-E1 cells in the bioprinted hydrogels on days 7 and 14. e) Representative fluorescence microscopy images of live/dead staining of the bioprinted hydrogels on days 1 and 7. (Live: green, dead: red). f) Representative fluorescence microscopy images of the cytoskeleton staining of the bioprinted hydrogels on days 1 and 7. (F-actin: green, nuclei: blue). Statistical analysis: $^{*}p < 0.05$, $^{**}p < 0.01$, and $^{***}p < 0.001$, $n = 3$. Scale bars for Figure 5e,f: 200 µm.

(0.222 ± 0.033 ng ng^{-1} (to total DNA)), Mp (0.166 ± 0.075 ng ng^{-1} (to total DNA)), and Hp_ATPE (0.226 ± 0.073 ng ng^{-1} (to total DNA) hydrogels, all significantly outperforming the non-pCNF containing hydrogels (0.073 ± 0.021 and 0.086 ± 0.065 ng ng^{-1} to total DNA for bulk and ATPE hydrogel, respectively). This suggests that the pCNF functioned as a signaling cue that is similar to the natural bone matrix and might help in promoting cell attachment, upregulation of osteogenic differentiation, and mineralization. Furthermore, pCNF's effect could be mediated by modulation of the mechanical stiffness of the hydrogel network that provided biophysical cues for osteogenic differentiation. Previous studies have demonstrated that the hydrogel stiffness strongly influences the cell fate, especially in the osteogenesis of mesenchymal stem cells, which occurs predominantly at an intermediate Young's modulus ≈30 kPa.[59–61] However, achieving a balance between optimal stiffness and printability is challenging, as less dense and relatively soft networks can compromise printability. In our study, adding less than 0.1% of pCNF could adjust the stiffness of ATPE hydrogel from ≈69 to ≈39 kPa, which might be a better fit for osteogenic differentiation.

The bone formation process, namely ossification, results in a tissue composed of bone cells and inorganic minerals in organic ECM. The results from cell viability and ALP enzyme activity assay indicated that the p_ATPE hydrogels promoted cell attachment and proliferation, while also stimulating early osteogenic responses. We conducted ARS staining to establish whether the ALP activity resulted in biomineralization and to see how calcium was incorporated in ATPE hydrogels. Cells that were laden in either the ATPE-based hydrogel or the Ca^{2+}(X) ATPE-based hydrogels were cultured for 21 days under normal growth conditions or osteogenic stimulus in standard. The hydrogels were sectioned with a cryostat and imaged with an optical microscope to obtain the morphology of the mineral nodules to avoid non-specific staining. Biomineralization was clearly demonstrated in **Figure 6**a across all hydrogels and culture conditions, with the staining specific to cell-containing samples, with no staining or dye precipitation for cell-free control samples. The mineralization in osteogenic medium (OM) without prior Ca^{2+} crosslinking had the weakest intensity and it propagated only to the vicinity of the cells generating only small precipitation centers (Figure 6a(i)). In Figure 6a(i), no multicellular biomineralized nodules were observed in the hydrogels cultured in OM without Ca^{2+} crosslinking. It is indicated that the cellular output of CaP was not sufficient to initiate precipitation within the timeframe of 21 days without Ca^{2+} crosslinking.

With the incorporation of pCNF in the ATPE hydrogels, the mineral formation by the cells was slightly enhanced when the hydrogels were Ca^{2+} crosslinked, as evidenced by the formation of large multicellular mineralized nodules (Figure 6a(ii) and (iii)). As expected, the strong osteogenic stimulus by OM increased biomineralization in relation to growth medium (GM). Under the OM incubation, there were more mineralized deposits in the Ca^{2+}(X) hydrogels (Figure 6a(iii),b). Interestingly however, the nodular morphology of the biomineralization was facilitated by the Ca^{2+} crosslinked pCNF network (Figure 6). These results suggest that the strongest biomineralization takes place when all inducers, pCNF, Ca^{2+} crosslinking, and OM treatment are applied synergistically.

Without prior Ca^{2+} crosslinking, the osteoblasts in Lp and Hp_ATPE hydrogels expressed similar ALP enzyme activity levels when cultured in GM (Figure 5d). However, in OM the biomineralization of the Ca^{2+}(X) hydrogels was significantly higher in the Lp_ATPE hydrogels (Figure 6c). This supports the interpretation that the cells' differentiation of activity is not impacted by the available Ca^{2+}, but rather the chemical microenvironment does not favor precipitation without added Ca^{2+}. It was also previously reported elsewhere that there is no direct correlation between the ALP and mineralization levels.[62,63]

This might be associated with the stoichiometric condition of the surface phosphates and the uptaken Ca^{2+} ions during the secondary crosslinking step in this sample series. We anticipate that for Lp_ATPE, the combined concentration profiles of surface phosphate and the Ca^{2+} ions initially within the macroporous hydrogel might favor the cellular biomineralization response the most. Therefore, Hp_ATPE composition would have more phosphates to coordinate Ca^{2+} and this competition results in fewer biomineralized nodules. The Ca^{2+}-coordinating effect of ECM-components might have ramifications for the design of 3D models even in other Ca^{2+}-sensitive organoid models.[62,63]

The role of non-collagenous proteins in the mineralization process is well known. One of these most common proteins produced by osteoblasts is osteocalcin (OCN). Even though there are controversies about the role of osteocalcin in bone mineralization, some research reports suggest that osteocalcin has an inhibitory effect on the mineralization of bone.[64,65] The highest OCN expression and lowest mineralization observed (Figures 6 and 7) for the cells in Hp_ATPE hydrogels in our research might be due to this control mechanism at the molecular level. Nevertheless, our results demonstrated that especially the Lp_ATPE hydrogels with prior Ca^{2+} ion crosslinking induced a pronounced in vitro biomineralization when incubated in OM.

To explain the mineralization data we proceeded with transcription analysis to understand how the material affects osteoblasts' differentiation. The expression analysis was done on days 7 and 14 in cultures grown in GM, i.e., without osteogenic stimulus, in Ca^{2+}(X) hydrogels. We have evaluated the relative expression levels of a panel of genes describing the osteogenic and chondrogenic differentiation of preosteoblastic mesenchymal stem cells, the MC3T3-E1s. We observed a significant upregulation of chondrogenic SRY-Box Transcription Factor 9 (Sox9) in samples grown in Hp_ATPE hydrogels for 14 days. We compared the pCNF-containing p_ATPE hydrogels to the plain ATPE hydrogel. This would be consistent mesenchymal cell condensation, chondrogenesis, and endochondral ossification typical for fracture healing.[66] Furthermore, we detected a general trend of osteogenic gene expression that had a positive correlation with pCNF concentration in the hydrogels. We observed the highest increase in the expression levels of ALP (alkaline phosphatase), Col1a1 (collagen type I alpha 1 chain), DMP1 (dentin matrix acidic phosphoprotein 1), and OCN (osteocalcin, BGLAP, bone gamma-carboxyglutamate protein) for Hp_ATPE hydrogels, which had the highest pCNF content, on day 7. Only for the Sp7 (Osterix) gene, the expression level for Mp_ATPE hydrogel was slightly higher than Hp_ATPE hydrogel at the same time point. The relative expression for all osteogenic and chondrogenic genes, except Sp7, continued to increase when cultures reached day 14. Sp7 is a transcription factor and activates the

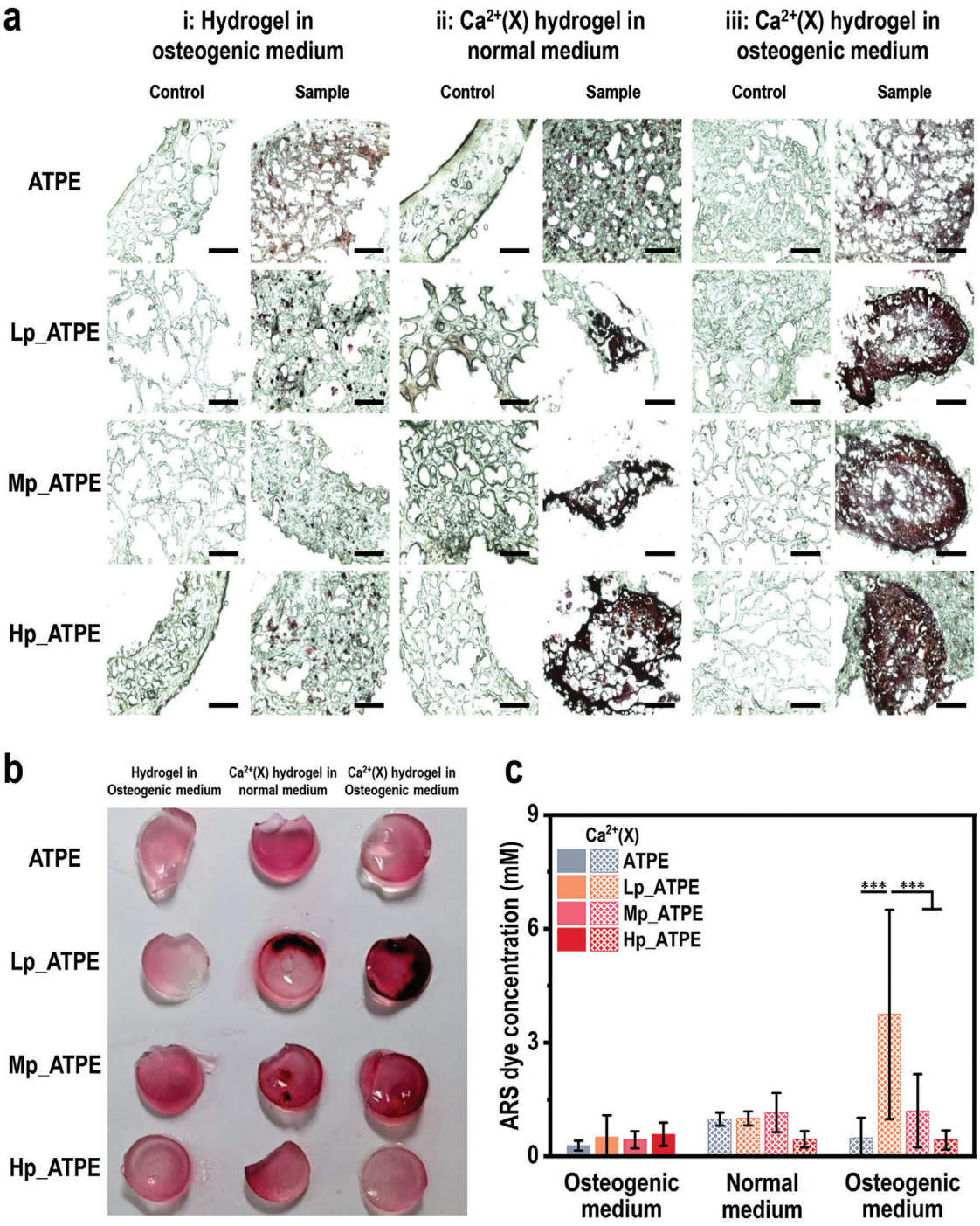

Figure 6. Detection of ECM mineralization. a) Optical microscopy images of the cryosections of the ARS stained hydrogels on day 21. b) Representative images of the ARS stained hydrogels on day 21. c) Quantification of ARS dye concentration of the stained hydrogels using the CPC method. Statistical analysis: $^{***}p < 0.001$, $n = 3$. Scale bars for Figure 6a: 400 μm.

expression of osteogenesis-related genes in pre-osteoblasts. The relative decrease in the expression level of Sp7 on day 14 for Mp_ATPE and Hp_ATPE hydrogels compared to day 7 might be due to the completion of its role after switching on the expression of other osteoblastic genes. Since no additional osteogenic inducers have been used, the increase in osteoblastic gene expressions arose from the incorporation of pCNF and also the interaction of Ca^{2+} with pCNF.

We were initially perplexed by the seemingly contraindicatory data on optimal pCNF concentration, highest osteogenic gene expression in Hp_ATPE hydrogels, and highest functional biomineralization in Lp_ATPE hydrogels. Even without osteogenic

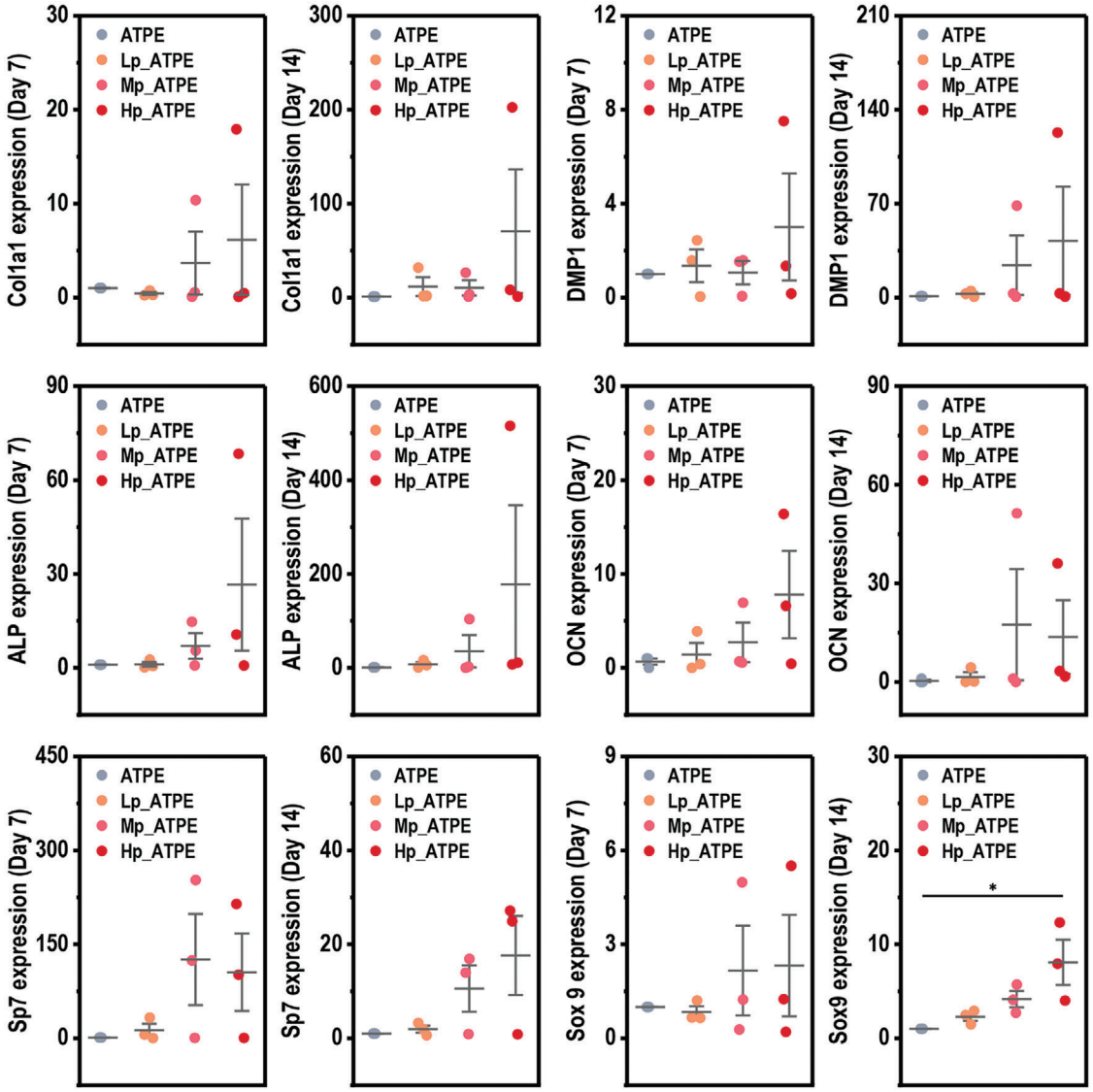

Figure 7. Assessment of gene expression level. Expression analysis of osteogenesis-related markers (Col1a1, DMP1, ALP, OCN, and Sp7) and chondrogenesis-related marker (Sox9) in the Ca^{2+}(X) ATPE-based hydrogels cultured in GM for 7 and 14 days. Statistical analysis: $^{*}p < 0.05$, $n = 3$.

stimulus biomineralization was more abundant in Lp_ATPE than in Hp_ATPE cultured under strong osteogenic stimulus. Pi has been shown to stimulate heterotrophic ossification through the Akt/mTOR pathway.[66–69] This process, reminiscent of physiological Pi storage in calcified tissues, can explain the upregulation of osteogenic genes. Intriguingly, in our hydrogels, the upregulation of osteogenic genes was accompanied by Sox9 (**Figure 7**), alluding to more regulated ossification than the heterotopic accumulation of minerals that are associated with pathological processes, a conclusion supported by the sectioned hydrogels (Figure 6). The biomineralization patterns observed may be partly regulated by the organization of pCNF at the GelMA-phase surface and the abundance of nucleation sites at the interface. Furthermore, this interface provides also a mechanical cue between rigid and soft ECM (Figure 4). The lower biomineralization despite higher osteogenic induction is likely a result of the pCNF network's un-saturated Ca^{2+} crosslinking and ability to sequester more Ca^{2+} into the network, thereby competing with the biomineralization process (Figure 6).

3. Conclusion

In summary, we present a pCNF-incorporated dextran/GelMA ATPE bioink system for extrusion-based bioprinting of MC3T3-E1 cells to fabricate macroporous hydrogels that promote mineralization and osteogenic differentiation. The pCNF is selectively partitioned into the GelMA phase in a low ion-strength buffer and forms a physically entangled network, which significantly enhances the stability of the ATPE bioink without hindering the macropore formation. The incorporation of pCNF could improve the rheological properties that benefit the bioprinting process of the ATPE bioink. When the bioink is photo-crosslinked,

the pCNF network showed better performance in energy dissipation during cyclic compression and improved the toughness and robustness of the macroporous hydrogels. The abundant surface phosphates on the pCNF functioned as local nucleation centers and accelerated biomineralization within the hydrogels when present in low quantities. Furthermore, the microenvironments within the macroporous hydrogel regulated the formation of structurally distinct mineralized nodules. The bioprinted hydrogels highlighted superior cell activity and ALP activity of MC3T3-E1 cells in the p_ATPE hydrogels. The p_ATPE hydrogels also promoted osteogenic and Sox9 gene expression intrinsically without added stimulants. On the whole, the pCNF greatly enhanced the overall properties of the ATPE bioink and endows the potential to serve in engineering in vitro 3D bone models.

4. Experimental Section

Materials and Chemicals: All the chemicals were purchased from Sigma-Aldrich unless otherwise stated.

Materials and Chemicals—pCNF Preparation: The phosphorylation of cellulose nanofibrils was performed according to a previously reported method with slight modification.[70] Initially, a microfibrillated cellulose film (hardwood pulp, diameter of 10 cm, dry mass of 1 g) was prepared by vacuum filtration and dried at room temperature overnight. Then the cellulose film was wetted with 1.8 mL solution containing $NH_4H_2PO_4$ (2.2 M) and urea (11.1 M) at room temperature overnight. To complete the phosphorylation process, the wet cellulose film was cured for 10 min at 165 °C and further dialysis against deionized (DI) water (cut-off: 14 kDa) for 7 days. Then the phosphorylated cellulose was defibrilized by high-pressure homogenization at 1000 bar for 10 passes to obtain the pCNF dispersion.

Materials and Chemicals—GelMA Preparation: GelMA was synthesized according to the previously reported method.[71] Briefly, 10 g of gelatin (Type A, 300 g bloom number) was dissolved into 100 mL PBS for 1 h at 50 °C. The methacrylation was performed by adding 8 mL of methacrylic anhydrite with a speed of 0.5 mL min^{-1}, and further reaction for 3 h at 50 °C. The reaction was quenched by adding 200 mL of PBS. The result solution was dialyzed against DI water (cut-off: 14 kDa) for 7 days at 40 °C, followed by lyophilization to obtain the GelMA powder.

Materials and Chemicals—ATPE Bioink Preparation and Characterizations: GelMA, dextran (Mw = 500 kDa, Alfa Aesar), pCNF, and lithium phenyl-2,4,6-trimethylbenzoylphosphinate (LAP, 0.25%) were mixed with a buffer containing HEPES (20 mM) and D-mannitol (160 mM) to the final concentrations, as listed in **Table 1**. The materials applied in cellular assays were sterilized either by filtration through a 0.22 µm nylon filter before lyophilization or autoclave at 125 °C for 30 min. Rheological analysis of the inks was carried out using an Anton Paar Physica MCR 702 rheometer (Anton Parr GmbH) with a parallel plate geometry (diameter: 25 mm, gap distance: 250 µm). The bioinks were pre-sheared at 100 s^{-1} for 20 s and equilibrium for 60 s before testing. The viscosity curves of the inks at 15 and 25 °C were measured by shear flow measurement with a shear rate ramping from 0.05 to 1000 s^{-1}. For quantitative analysis of the flow behavior of the inks under 15 and 25 °C, the flow curves were fitted into the power law model to obtain power law index n and consistency coefficient k. The temperature-dependent behavior of the inks was determined by an oscillatory temperature sweep from 40 to 5 °C with a rate of 1.5 °C min^{-1}. The shear strain and frequency were fixed at 0.1% and 5 Hz, respectively. The shear recovery properties were characterized using oscillatory step tests at 15 °C by shearing the sample at 0.1% and 1.5 Hz for 30 s, followed by increasing the strain to 500% for 10 s and then recovering the strain to 0.1% strain for 30 s. The strain ramp up and down was repeated twice in one measurement. Photo-rheological analysis was performed to measure the crosslinking response under oscillation mode at a constant oscillatory strain and frequency of 0.1% and 1.5 Hz, respectively. A blue light source (λ = 405 nm, 15 mW cm^{-2}, bluepoint LED eco, Hönle Group) started irradiation upon the samples through a transparent bottom plate after 30 s. The change in storage modulus (G') was recorded at 15 °C. All measurements were carried out at least in triplicate. The stability of the inks was monitored using a Turbiscan Lab Expert stability analyzer (Formulation) equipped with a pulsed near-infrared light source (λ = 880 nm) with 60 s per scan for 12 h at 37 °C (physiological temperature). The inks were mixed properly and equilibrium at 37 °C for 10 min before scanning. The turbiscan stability index (TSI) value was calculated using the transmitted signals of the test samples along the sample height to compare their stability. A TSI value lower than 3 indicates the destabilization of ink is in an early stage, but over 90% of the destabilization is not visual. A TSI value greater than 10 indicates the destabilization corresponding to sedimentation/creaming and phase separation of the ink is visible. The morphology of the inks and the pCNF partition behavior within the ATPE-based inks were characterized using a 3i Marianas CSU-W1 spinning disk confocal microscope (50 µm pinholes, Intelligent Imaging Innovations GmbH) with 33 steps in Z direction and 3.01 µm between each step. The testing samples were prepared by replacing GelMA and dextran with 1% w/w Rhodamine B conjugated GelMA (R-GelMA) and FITC dextran (Mw = 500 kDa) based on the GelMA and dextran weight, respectively.[72] The pCNF was further stained by adding calcofluor white (25 mM) and incubating at 37 °C for 30 min before imaging. To understand the influence of monocations on the emulsion morphology and pCNF partition, all ATPE-based inks prepared using PBS were also characterized.

Materials and Chemicals—Hydrogel Preparation and Characterizations: Hydrogel cylinders (diameter: ≈4.5 mm, height: ≈3.5 mm) for mechanical properties measurements were crosslinked (λ = 405 nm, 15 mW cm^{-2}) for 5 min. The mechanical compression test was performed using a dynamic mechanical analyzer (MCR 702 Multidrive, Anton Paar GmbH) at room temperature. A 10 mN preload was set to ensure complete contact between the casted hydrogel cylinder and the measuring plate. Hydrogel cylinders were compressed at a constant speed of 2 mm min^{-1}. Young's modulus was calculated by linear fitting of the initial elastic region (0–10%) of the stress–strain curves. The Ca^{2+} crosslinked (Ca^{2+} (X)) hydrogels were prepared by soaking the hydrogel cylinders in 100 mM calcium chloride solution for 1 min. High-strain cyclic compression test was performed to understand the influence of pCNF on the cyclic performance, the hydrogels were applied with 40% strain compression with a rate of 10% strain s^{-1} for 100 cycles. The SEM images were captured using an LEO 1530 SEM equipped with an attached energy dispersive X-ray spectrometer (EDX) detector at an accelerating voltage of 5.0 kV. The hydrogel cylinders were incubated in PBS for 24 h and DI water for 24 h at room temperature until dextran leached and reached equilibrium. The cross-sectional samples were prepared using the freeze-fracture method in liquid nitrogen. The mineralization ability of the hydrogels was evaluated according to a reported method with slight modifications.[73] The washed hydrogel discs were immersed in 10X SBF at 37 °C and incubated in an orbital shaker (S1500, Stuart) at 90 rpm for 6 h. Subsequently, the hydrogels were rinsed thoroughly with DI water, followed by a gradual solvent exchange with ethanol. They were then lyophilized by a critical point dryer (Leica EM CPD300, Leica) to obtain samples for visualization of the surface structure and mineral precipitates.

Materials and Chemicals—3D printing: 3D printing demo was performed using a multitool 3D bioprinter (Brinter ONE, Brinter) equipped with an air-pressure controlled dispensing tool (Pneuma Tool Cooled,

Table 1. The formulation composition of the bioinks.

Inks	GelMA [% w/v]	Dextran [% w/v]	pCNF [% w/v]
Bulk ink	8	0	0
ATPE ink	8	2	0
Lp_ATPE ink	8	2	0.05
Lp_ATPE ink	8	2	0.075
Lp_ATPE ink	8	2	0.1

Brinter). The Lp_ATPE ink was loaded into a 3 mL light-proof syringe (Amber Barrels, Nordson) equipped with a precision stainless steel tip (25 gauge, Nordson). The Lp_ATPE ink was pre-cooled at 4 °C for 10 min and equilibrated at printing temperature for 10 min before printing. The 3D printing was performed with a constant speed of 3 mm s^{-1}, a layer height of 0.25 mm, a pressure in the range of 1950–2150 mbar, and a temperature of 15 °C. After printing, the human ear, X-, and Y-shaped hollow tube hydrogels were crosslinked ($\lambda = 405$ nm, 15 mW cm^{-2}, 60 s), and soaked in PBS. The X-tube hydrogels were photo-crosslinked ($\lambda = 405$ nm) every 20 layers for 10 s during the printing. The printability of each ink was determined according to a published method, by printing 4-layered crosshatch scaffolds and analyzing the perimeter and area of interconnected channels.[56] The printability value (Pr) was determined by the below equation:

$$\mathrm{Pr} = \frac{L^2}{16A} \quad (1)$$

Where L indicates the perimeter and A indicates the area.

Cell Culture: MC3T3-E1 cells were cultured using a complete cell culture medium containing minimum essential medium α (MEM α) supplemented with FBS (10%), glutaMAX (2 mM), and Pen-strep (100 U mL^{-1}). MC3T3-E1 cells were passaged about once a week, and the cell culture medium was replaced twice a week. All the cells were cultured in a humidified incubator with a CO_2 atmosphere (5%) at a constant temperature of 37 °C.

Cell Culture—Bioprinting: MC3T3-E1 cells before passage 14 were harvested and resuspended within the inks (warmed up at 37 °C) by gentle pipetting to achieve a cell density of 1.5×10^6 cells mL^{-1}. Bioprinting was performed using a multitool 3D bioprinter (Brinter ONE, Brinter) equipped with an air-pressure controlled dispensing tool (Pneuma Tool Cooled, Brinter). The bioinks were loaded into a 3 mL light-proof syringe (Amber Barrels, Nordson) equipped with a precision stainless steel tip (25 gauge, Nordson). The bioinks were pre-cooled at 4 °C for 10 min and equilibrated at printing temperature for 10 min before bioprinting. The bioprinting for all bioinks was performed under similar conditions with a constant speed of 3 mm s^{-1}, a pressure in the range of 1675–2300 mbar, and a temperature in the range of 15–21 °C. Hydrogels (6 mm in diameter, 3 layers) were printed onto a 10 cm petri dish and further photo-crosslinked ($\lambda = 405$ nm, 15 mW cm^{-2}, 30 s) before transferring to the non-cell culture treated 96 well plates and incubated at 37 °C and 5% CO_2 in the cell culture medium.

Cell Culture—Cytocompatibility and Viability Analysis: MC3T3-E1 cells before passage 14 (counting from the original ATCC line) were harvested and resuspended within the inks (warmed up at 37 °C) by gently pipetting to achieve a cell density of 1.5×10^6 cells mL^{-1}. Fifty microliters of the bioinks were added into the non-cell culture-treated 96 well plates and crosslinked using a large-format curing light source ($\lambda = 405$ nm, 15 mW cm^{-2}, 30 s) to eliminate factors unrelated to the material properties. The cell-laden hydrogels were cultured at 37 °C and 5% CO_2 in the cell culture medium, and the cell proliferation was determined using CCK-8 assay on days 1, 3, and 7.

Cell viability within the bioprinted hydrogels was determined on days 1, 3, and 7 by the Live/Dead assay using the Live/Dead Cell Staining Kit II (Promocell) to evaluate the impact of the bioprinting process. Briefly, the bioprinted hydrogels were washed using PBS and cultured using a testing agent (0.5 µM Calcein-AM/1.6 µM EthD-III in PBS) at room temperature for 1 h. The fluorescence microscopy images of the bioprinted cells were obtained using a 3i Marianas CSU-W1 spinning disk confocal microscope (50 µm pinholes, Intelligent Imaging Innovations GmbH) with 50 steps in Z direction and 3.01 µm between each step. Cell viability was quantitatively determined by Fiji software.

Cell Culture—Nuclear and Cytoskeletal Staining: For observation of cell-material interactions, MC3T3-E1 cells within bioprinted hydrogels were stained with Alexa Fluor 488 Phalloidin (Cell Signaling Technology) and DAPI (Cayman Chemicals) for actin filaments and the nuclei, respectively. Briefly, bioprinted hydrogels were permeabilized with 0.2% Triton X-100 for 10 min at room temperature, washed with PBS, and further incubated with 1% BSA for 1 h at room temperature. Then, BSA was replaced by 165 nM Alexa Fluor 488 Phalloidin and incubated for 30 min at room temperature, followed by staining with 259 nM DAPI for 15 min. The morphology of the bioprinted cells was captured using a 3i Marianas CSU-W1 spinning disk confocal microscope (50 µm pinholes, Intelligent Imaging Innovations GmbH) with 33 steps in Z direction and 3.01 µm between each step.

Cell Culture—Assessment of ALP Enzyme Activity: ALP enzyme activity of the bioprinted MC3T3-E1 cells was determined using SensoLyte pNPP Alkaline Phosphatase Assay Kit Colorimetric (AnaSpec) according to the manufacturer's instructions. Briefly, at each time point, the bioprinted hydrogels were washed with PBS before transferring to the microcentrifuge tubes and homogenized in the assay buffer that was provided in the kit. After centrifuging at 10 000 g and 4 °C for 15 min, the supernatant from homogenized samples was transferred to a 96-well plate and incubated with pNPP substrate at 37 °C for 1 h. The reaction was stopped by the addition of stop solution and the absorbance was read at 405 nm with a plate reader (VarioSkan Flash, Thermo Scientific). The ALP enzyme standard curve was obtained by reaction of pNPP with different concentrations of ALP enzyme from the bovine intestine, which was supplied by the manufacturer, under the same conditions as the samples. The absorbance of the samples was expressed as ng ALP enzyme by using the standard curve.

The total DNA amount was determined with Quant-iT PicoGreen dsDNA Reagent (Invitrogen) according to the manufacturer's instructions. Briefly, 1 volume of 10 mM Tris-HCl, 1 mM EDTA (pH = 5) buffer was added to the sample homogenates and this dilution was further mixed with PicoGreen Reagent in a volume ratio of 1:1 in a 96-well plate and incubated at room temperature for 5 min protected from light. Then the fluorescence intensity was measured with a plate reader (VarioSkan Flash, Thermo Scientific) at 480 nm excitation and 520 nm emission. The DNA concentration was quantified from a curve plotted with a known DNA standard sample. The ALP content of each sample was normalized to DNA content and the results were expressed as $ng_{ALP}\ ng_{DNA}{}^{-1}$.

Cell Culture—Detection of ECM Mineralization: ECM mineralization of MC3T3-E1 cells within hydrogels cultured under different conditions was detected by Alizarin red S (ARS, Thermo Scientific Chemicals) staining. Briefly, cell-laden hydrogels and Ca^{2+}(X) hydrogels were cultured in normal and osteogenic medium for 21 days. Then, the cell-laden hydrogels were fixed with 4% PFA, washed with distilled water, and stained with ARS (2%) at 37 °C for 30 min. Microscope images were taken with an EVOS microscope (Thermo Fischer Scientific) and the quantitation of staining was done by cetylpyridinium chloride (CPC) extraction method. Briefly, stained and washed hydrogels were transferred to a clean 96-well plate and incubated in 10% CPC in 10 mM sodium phosphate solution (pH 7) for 1 h on a plate shaker at room temperature. The dye released from the samples with CPC was transferred to a 96-well plate and the absorbance was measured at 562 nm with a plate reader (VarioSkan Flash, Thermo Scientific). A standard curve was plotted with the absorbance versus ARS dye concentration and the results were expressed as mM ARS dye released from the samples.

The cell-laden hydrogels were also sectioned for microscopy with a cryostat (Leica CM 3050 S). Before cryosectioning, the ARS stained samples were frozen in Tissue-Tek O.C.T. Compound (Sakura Finetek) at −70 °C. Samples were sectioned at −20 °C with a thickness of 20 µm.

Cell Culture—Assessment of Osteoblastic Gene Expression Levels by qRT-PCR: The osteoblastic differentiation of MC3T3-E1 cells within the Ca^{2+}(X) hydrogels was determined by expression levels of several osteoblast-specific genes. RNA was isolated from the hydrogels on days 7 and 14 using TRIzol reagent (Invitrogen, Thermo Fisher Scientific). The concentration and purity of sample RNAs were measured with a nanodrop spectrophotometer (NanoDrop 2000c, Thermo Fischer Scientific). mRNAs were later converted to cDNAs by iScript cDNA synthesis kit (Bio-Rad) by using 500 ng RNA as the template for each sample. Quantitative reverse transcription polymerase chain reaction (qRT-PCR) was performed by using iTaq Universal SYBR Green Supermix kit (Bio-Rad) and the reaction was performed in an optical thermal cycler (Bio-Rad CFX96). The primer sequences used for qPCR are listed below. PCR reaction was

Table 2. Gene primer pairs used in the RT-qPCR.

Genes	Primer sequences
Col1a1	Forward: CGATGGATTCCCGTTCGAGT Reverse: CGATCTCGTTGGATCCCTGG
DMP1	Forward: CAGTGAGGATGAGGCAGACA Reverse: CGATGCTCCTGGTACTCTC
ALP	Forward: CCAGCAGGTTTCTCTCTTGG Reverse: GGGATGGAGGAGAGAAGGTC
OCN	Forward: CTTGGTGCACACCTAGCAGA Reverse: CCCAAAGAAATGAACCAGGA
Sp7	Forward: TGGAGAGGGAAAGGGATTCT Reverse: TCGGAGACCTCGAGGATAGA
Sox9	Forward: CACACGTCAAGCGACCCATGAA Reverse: TCTTCTCGCTCTCGTTCAGCAG
CLPH	Forward: CAGATCGAGGGATCGATTCAG Reverse: TCACCACTTGACACCCTCATTC

performed with the following steps: Denaturation (95 °C for 3 min), followed by 10 cycles of annealing by touchdown method starting with 63 °C with 0.5 °C decrease in each cycle, and extension at 72 °C for 15 s, followed by 30 repeats of [95 °C for 10 s, followed by 57 °C for 15 s, and 72 °C for 15 s] cycles, in a reaction volume of 20 µL on opaque full-skirted 96-well PCR plates (VWR).

The relative expression levels of the target genes were calculated by threshold cycle (ΔΔCt) method with CLPH as the housekeeping reference gene and reported as $2^{-\Delta\Delta Ct}$. ATPE hydrogels were used as the control. The primer sequences and genes are listed in **Table 2**.

Statistical Analysis: The statistical analysis of material characterization was performed using one-way or two-way analysis of variance (ANOVA), at least three measurements were performed and the results were displayed as mean ± standard deviation. All the in vitro experiments were repeated as three technical and three biological replicates and the results were displayed as mean ± standard deviation. Comparisons between different groups for statistical analysis were done by ANOVA or two-way ANOVA, where applicable. Differences between groups for cell viability and ALP activity were demonstrated by ANOVA followed by Tukey's post hoc test. Significant differences were reported with $^{*}p < 0.05$, $^{**}p < 0.01$, and $^{***}p < 0.001$.

Supporting Information

Supporting Information is available from the Wiley Online Library or from the author.

Acknowledgements

Q.W. would like to acknowledge the financial support from the China Scholarship Council (Student ID 201907960002) and Business Finland Project (1529/31/2022) for his doctoral study at Åbo Akademi University (ÅAU), Finland. X.W. and Ö.K. would like to thank the Academy of Finland (333158) as well as the Jane and Aatos Erkko Foundation for their research funds. T.N. would like to thank the Olins Foundation within the Swedish Cultural Foundation in Finland and the Finnish Society for Sciences for supporting his research. J.M.R. and C.X. would like to acknowledge the Business Finland co-innovation project (575/31/2023). This research is also aligned with the strategic research profiling area "Solutions for Health" at Åbo Akademi University (funded by the Research Council/Academy of Finland, 336355). MSc. Liqiu Hu and Dr. Luyao Wang are respectively acknowledged for their help with sample preparation and assisting in the TEM characterization of pCNF. Parts of the research used the Research Council of Finland Research Infrastructure "Printed Intelligence Infrastructure" (PII-FIRI).

Conflict of Interest

The authors declare no conflict of interest.

Author Contributions

Q.W. and Ö.K. equally contributed to this work. X.W. and Q.W. conceived and initiated the work. Q.W. performed the experimental work on bioink formulation, rheological and mechanical characterizations, 3D bioprinting, and cytocompatibility and acted as the main writing author to coordinate the manuscript drafting with the other authorships. Ö.K. carried out the laboratory work on ALP, ARS staining, and gene expression by qRT-PCR. X.W. and T.N. co-supervised the research content. C.X. and J.M.R. provided critical revision and infrastructure support to the work. All authors contributed to experimental design, execution, data analysis, and manuscript revision. The manuscript has been approved by all the authors for submission.

Data Availability Statement

The data that support the findings of this study are available from the corresponding author upon reasonable request.

Keywords

aqueous two-phase emulsion, bioprinting, mineralization, osteogenic differentiation, phosphorylated cellulose nanofibrils

Received: January 9, 2024
Revised: February 22, 2024
Published online:

[1] I. Matai, G. Kaur, A. Seyedsalehi, A. McClinton, C. T. Laurencin, *Biomaterials.* **2020**, *226*, 119536.
[2] J. Zhang, Y. Chen, Y. Huang, W. Wu, X. Deng, H. Liu, R. Li, J. Tao, X. Li, X. Liu, M. Gou, *Adv. Sci.* **2020**, *7*, 2002601.
[3] Z. Luo, G. Tang, H. Ravanbakhsh, W. Li, M. Wang, X. Kuang, C. E. Garciamendez-Mijares, L. Lian, S. Yi, J. Liao, M. Xie, J. Guo, Z. Zhou, Y. S. Zhang, *Adv. Mater.* **2022**, *34*, 2108931.
[4] G. Ying, N. Jiang, C. Yu, Y. S. Zhang, *Bio-Design Manuf.* **2018**, *1*, 215.
[5] W. J. Kim, H. Lee, J. U. Lee, A. Atala, J. J. Yoo, S. J. Lee, G. H. Kim, *Biomaterials.* **2020**, *230*, 119632.
[6] A. R. Spencer, E. Shirzaei Sani, J. R. Soucy, C. C. Corbet, A. Primbetova, R. A. Koppes, N. Annabi, *ACS Appl. Mater. Interfaces.* **2019**, *11*, 30518.
[7] G. L. Ying, N. Jiang, S. Maharjan, Y. X. Yin, R. R. Chai, X. Cao, J. Z. Yang, A. K. Miri, S. Hassan, Y. S. Zhang, *Adv. Mater.* **2018**, *30*, 1805460.
[8] S. Yi, Q. Liu, Z. Luo, J. J. He, H. L. Ma, W. Li, D. Wang, C. Zhou, C. E. Garciamendez, L. Hou, J. Zhang, Y. S. Zhang, *Small.* **2022**, *18*, 2106357.
[9] K. Dubbin, A. Tabet, S. C. Heilshorn, *Biofabrication.* **2017**, *9*, 044102.
[10] B. Grigoryan, S. J. Paulsen, D. C. Corbett, D. W. Sazer, C. L. Fortin, A. J. Zaita, P. T. Greenfield, N. J. Calafat, J. P. Gounley, A. H. Ta, F. Johansson, A. Randles, J. E. Rosenkrantz, J. D. Louis-Rosenberg, P. A. Galie, K. R. Stevens, J. S. Miller, *Science.* **2019**, *364*, 458.
[11] P. N. Bernal, P. Delrot, D. Loterie, Y. Li, J. Malda, C. Moser, R. Levato, *Adv. Mater.* **2019**, *31*, 1970302.
[12] J. Esquena, *Curr. Opin. Colloid Interface Sci.* **2016**, *25*, 109.
[13] J. Tao, S. Zhu, N. Zhou, Y. Wang, H. Wan, L. Zhang, Y. Tang, Y. Pan, Y. Yang, J. Zhang, R. Liu, *Adv. Healthcare Mater.* **2022**, *11*, 2102810.

[14] M. Wang, W. Li, Z. Luo, G. Tang, X. Mu, X. Kuang, J. Guo, Z. Zhao, R. S. Flores, Z. Jiang, L. Lian, J. O. Japo, A. M. Ghaemmaghami, Y. S. Zhang, *Biofabrication*. **2022**, *14*, 024105.
[15] X. S. Qin, M. Wang, W. Li, Y. S. Zhang, *Regen. Eng. Transl. Med*. **2022**, *8*, 471.
[16] Q. Wang, Ö. Karadas, O. Backman, L. Wang, T. Näreoja, J. M. Rosenholm, C. Xu, X. Wang, *Adv. Healthcare Mater.* **2023**, *12*, 2203243.
[17] D. Klemm, F. Kramer, S. Moritz, T. Lindström, M. Ankerfors, D. Gray, A. Dorris, *Angew. Chem., Int. Ed*. **2011**, *50*, 5438.
[18] Q. Wang, O. Backman, M. Nuopponen, C. Xu, X. Wang, *Front. Chem. Eng*. **2021**, *3*, 723429.
[19] D. S. Naidu, M. J. John, *Int. J. Biol. Macromol*. **2021**, *179*, 448.
[20] H. Zhao, Y. Zhang, Y. Liu, P. Zheng, T. Gao, Y. Cao, X. Liu, J. Yin, R. Pei, *Biomacromolecules*. **2021**, *22*, 5097.
[21] H. Du, W. Liu, M. Zhang, C. Si, X. Zhang, B. Li, *Carbohydr. Polym*. **2019**, *209*, 130.
[22] A. Pandey, *Environ. Chem. Lett*. **2021**, *19*, 2043.
[23] C. Lei, Y. Xie, Y. Wu, Y. Li, B. Li, Y. Pei, S. Liu, *Food Hydrocoll*. **2022**, *130*, 107698.
[24] N. Broguiere, A. Husch, G. Palazzolo, F. Bradke, S. Madduri, M. Zenobi-Wong, *Biomaterials*. **2019**, *200*, 56.
[25] J. Malda, J. Visser, F. P. Melchels, T. Jüngst, W. E. Hennink, W. J. A. Dhert, J. Groll, D. W. Hutmacher, *Adv. Mater.* **2013**, *25*, 5011.
[26] E. Chang, J. Zhao, C. Zhao, G. Li, P. C. Lee, C. B. Park, *Chem. Eng. J*. **2022**, *438*, 134060.
[27] F. K. Lewns, O. Tsigkou, L. R. Cox, R. D. Wildman, L. M. Grover, G. Poologasundarampillai, *Adv. Mater.* **2023**, 2301670.
[28] P. S. Zieliński, P. K. R. Gudeti, T. Rikmanspoel, M. K. Włodarczyk-Biegun, *Bioact. Mater.* **2023**, *19*, 292.
[29] P. S. Gungor-Ozkerim, I. Inci, Y. S. Zhang, A. Khademhosseini, M. R. Dokmeci, *Biomater. Sci*. **2018**, *6*, 915.
[30] H. Zhu, M. Monavari, K. Zheng, T. Distler, L. Ouyang, S. Heid, Z. Jin, J. He, D. Li, A. R. Boccaccini, *Small*. **2022**, *18*, 2104996.
[31] J. Zhang, H. Eyisoylu, X. H. Qin, M. Rubert, R. Müller, *Acta Biomater.* **2021**, *121*, 637.
[32] C. Vater, P. Kasten, M. Stiehler, *Acta Biomater.* **2011**, *7*, 463.
[33] H. Lin, Y. Zhou, Q. Lei, D. Lin, J. Chen, C. Wu, *BMC Dev. Biol*. **2021**, *21*, 1.
[34] Y. R. V. Shih, Y. Hwang, A. Phadke, H. Kang, N. S. Hwang, E. J. Caro, S. Nguyen, M. Siu, E. A. Theodorakis, N. C. Gianneschi, K. S. Vecchio, S. Chien, O. K. Lee, S. Varghese, *Proc. Natl. Acad. Sci. U. S. A.* **2014**, *111*, 990.
[35] S. Rui, T. Kubota, Y. Ohata, K. Yamamoto, M. Fujiwara, S. Takeyari, K. Ozono, *Bone*. **2022**, *164*, 116525.
[36] W. J. Bae, Q. S. Auh, G. T. Kim, J. H. Moon, E. C. Kim, *Differentiation*. **2016**, *92*, 257.
[37] G. Cidonio, C. R. Alcala-Orozco, K. S. Lim, M. Glinka, I. Mutreja, Y. H. Kim, J. I. Dawson, T. B. F. Woodfield, R. O. C. Oreffo, *Biofabrication*. **2019**, *11*, 035027.
[38] S. Patil, N. Singh, *Biomater. Sci*. **2019**, *7*, 4687.
[39] J. Jeong, J. H. Kim, J. H. Shim, N. S. Hwang, C. Y. Heo, *Biomater. Res*. **2019**, *23*, 1.
[40] L. Liu, Y. Miao, X. Shi, H. Gao, Y. Wang, *ACS Biomater. Sci. Eng*. **2020**, *6*, 1500.
[41] L. Liu, Y. He, X. Shi, H. Gao, Y. Wang, Z. Lin, *Appl. Mater. Today*. **2018**, *12*, 21.
[42] S. Guo, Y. Zhu, W. Xu, S. Huan, J. Li, T. Song, L. Bai, O. J. Rojas, *Carbohydr. Polym*. **2023**, *299*, 120154.
[43] W. Xu, B. Z. Molino, F. Cheng, P. J. Molino, Z. Yue, D. Su, X. Wang, S. Willför, C. Xu, G. G. Wallace, *ACS Appl. Mater. Interfaces*. **2019**, *11*, 8838.
[44] L. Tea, T. Nicolai, F. Renou, *Langmuir*. **2019**, *35*, 9029.
[45] Q. Wang, W. Xu, R. Koppolu, B. van Bochove, J. Seppälä, L. Hupa, S. Willför, C. Xu, X. Wang, *Carbohydr. Polym*. **2022**, *276*, 118780.
[46] P. Fisch, N. Broguiere, S. Finkielsztein, T. Linder, M. Zenobi-Wong, *Adv. Funct. Mater.* **2021**, *31*, 2008261.
[47] J. Lewicki, J. Bergman, C. Kerins, O. Hermanson, *Bioprinting*. **2019**, *16*, e00053.
[48] K. Na, S. Shin, H. Lee, D. Shin, J. Baek, H. Kwak, M. Park, J. Shin, J. Hyun, *J. Ind. Eng. Chem*. **2018**, *61*, 340.
[49] S. M. Hull, L. G. Brunel, S. C. Heilshorn, *Adv. Mater.* **2022**, *34*, 2103691.
[50] M.-C. Li, Q. Wu, R. J. Moon, M. A. Hubbe, M. J. Bortner, M.-C. Li, Q. Wu, M. Li, R. J. Moon, M. A. Hubbe, M. J. Bortner, *Adv. Mater.* **2021**, *33*, 2006052.
[51] H. Zhang, Y. Cong, A. R. Osi, Y. Zhou, F. Huang, R. P. Zaccaria, J. Chen, R. Wang, J. Fu, *Adv. Funct. Mater.* **2020**, *30*, 1910573.
[52] J. Zeng, L. Jia, D. Wang, Z. Chen, W. Liu, Q. Yang, X. Liu, H. Jiang, *Int. J. Bioprinting*. **2023**, *9*, 131.
[53] K. Markstedt, A. Mantas, I. Tournier, H. Martínez Ávila, D. Hägg, P. Gatenholm, *Biomacromolecules*. **2015**, *16*, 1489.
[54] M. F. Cortes Ruiz, Y. Brusentsev, S. B. Lindström, C. Xu, L. Wågberg, *Carbohydr. Polym*. **2023**, *315*, 120950.
[55] Y. Fan, Z. Yue, E. Lucarelli, G. G. Wallace, *Adv. Healthcare Mater.* **2020**, *9*, 2001410.
[56] L. Ouyang, R. Yao, Y. Zhao, W. Sun, *Biofabrication*. **2016**, *8*, 035020.
[57] M. Dadsetan, M. Giuliani, F. Wanivenhaus, M. Brett Runge, J. E. Charlesworth, M. J. Yaszemski, *Acta Biomater.* **2012**, *8*, 1430.
[58] P. Müller, U. Bulnheim, A. Diener, F. Lüthen, M. Teller, E. D. Klinkenberg, H. G. Neumann, B. Nebe, A. Liebold, G. Steinhoff, J. Rychly, *J. Cell. Mol. Med.* **2008**, *12*, 281.
[59] N. Huebsch, P. R. Arany, A. S. Mao, D. Shvartsman, O. A. Ali, S. A. Bencherif, J. Rivera-Feliciano, D. J. Mooney, *Nat. Mater.* **2010**, *9*, 518.
[60] L. Ouyang, J. P. K. Armstrong, Y. Lin, J. P. Wojciechowski, C. Lee-Reeves, D. Hachim, K. Zhou, J. A. Burdick, M. M. Stevens, *Sci. Adv.* **2020**, *6*, 5529.
[61] S. J. Tan, J. Y. Fang, Z. Yang, M. E. Nimni, B. Han, *Biomaterials*. **2014**, *35*, 5294.
[62] C. D. Hoemann, H. El-Gabalawy, M. D. McKee, *Pathol. Biol*. **2009**, *57*, 318.
[63] B. Hoac, T. Kiffer-Moreira, J. L. Millán, M. D. McKee, *Bone*. **2013**, *53*, 478.
[64] M. L. Zoch, T. L. Clemens, R. C. Riddle, *Bone* **2016**, *82*, 42.
[65] P. G. F. van de Loo, B. A. M. Soute, L. J. M. van Haarlem, C. Vermeer, *Biochem. Biophys. Res. Commun.* **1987**, *142*, 113.
[66] S. Hasegawa, H. Kitoh, B. Ohkawara, K. Mishima, M. Matsushita, A. Masuda, N. Ishiguro, K. Ohno, *Biochem. Biophys. Res. Commun.* **2016**, *470*, 356.
[67] H. Zhou, G. Jiao, M. Dong, H. Chi, H. Wang, W. Wu, H. Liu, S. Ren, M. Kong, C. Li, L. Zhang, Y. Chen, *Biol. Trace Elem. Res.* **2019**, *190*, 327.
[68] L. Chen, M. Tian, J. Yang, Z. Wu, *Int. J. Mol. Sci*. **2023**, *24*, 15403.
[69] D. Mao, K. Wang, H. Jiang, J. Mi, X. Pan, G. Zhao, Y. Rui, *Am. J. Pathol*. **2024**, *194*, 430.
[70] Y. Noguchi, I. Homma, T. Watanabe, *Cellulose*. **2020**, *27*, 2029.
[71] C. D. O'Connell, C. D. Bella, F. Thompson, C. Augustine, S. Beirne, R. Cornock, C. J. Richards, J. Chung, S. Gambhir, Z. Yue, J. Bourke, B. Zhang, A. Taylor, A. Quigley, R. Kapsa, P. Choong, G. G. Wallace, *Biofabrication*. **2016**, *8*, 015019.
[72] X. Chen, Z. Yue, P. C. Winberg, Y. R. Lou, S. Beirne, G. G. Wallace, *Biomater. Sci*. **2021**, *9*, 2424.
[73] B. W. M. de Wildt, R. van der Meijden, P. A. A. Bartels, N. A. J. M. Sommerdijk, A. Akiva, K. Ito, S. Hofmann, *Adv. Funct. Mater.* **2022**, *32*, 2206992.